FIN THERMOELECTRIC COOLER PERFORMANCE CHARACTERIZATION

A Thesis
Presented to
The Academic Faculty

by

Patrick Lawrence Creamer

In Partial Fulfillment
of the Requirements for the Degree
Master of Science Mechanical Engineering in the
George W. Woodruff School of Mechanical Engineering

Georgia Institute of Technology
August 2018

FIN THERMOELECTRIC COOLER PERFORMANCE CHARACTERIZATION

Approved by:

Dr. Shannon Yee, Advisor
School of Mechanical Engineering
Georgia Institute of Technology

Dr. Samuel Graham
School of Mechanical Engineering
Georgia Institute of Technology

Dr. Todd Sulchek
School of Mechanical Engineering
Georgia Institute of Technology

Date Approved: July 24th, 2018

To the Blessed Mother.

ACKNOWLEDGEMENTS

First, I would like to thank God for the providing the grace to complete my degree and this thesis. I am incredibly grateful for my time at Georgia Institute of Technology and all the blessings I have received here. It has been an incredibly transformative experience, in many ways that I did not anticipate. I would like to thank my advisor, Dr. Shannon Yee, for his support and encouragement. I also offer my sincere gratitude to my committee members, Dr. Samuel Graham and Dr. Todd Sulchek for their support. I am incredibly grateful to my lab mates for their support and guidance, most especially to Sampath Kommandur, for his ever-willingness to offer advice for my project, and the countless hours he devoted to checking derivations. Additionally, to Dr. Andrey Gunawan, Misha Rodin, Aravindh Rajan, Jong Ha, Alexander Limia, Akanksha Menon (The Kankanator), Shawn Gregory, and Venkatesh Chinnakonda. I would also like to thank our sponsor, Silniva, John Carberry, and Devin Roberts. A sincere thanks is also due to the Georgia Tech clean room staff, especially Chris Yang for his support. It has been a blessing to work with everyone in CNES, as lab boundaries have often overlapped as people sought to help each other. I would especially like to thank Hamidreza Seyf for his fluid dynamics modeling insight.

From the bottom of my heart, I would most especially like to my family, and all of my friends who have supported me along the way. Especially, my parents, David and Margaret Creamer, my brothers and sisters, David, Ryan, Jack, Matthew, Kelly, Katie, and Mary. Additionally, all my friends who have suffered through grad school with me including Michael Griffin, Samuel Petter (The Stallion), David Arellano, Alejandro Barrios, Esteban

Carillo, Giovanni Maronati, Aaron Mebane, Matheus Nora Rosa, the Missionaries of Charity, and the entire Georgia Tech Catholic Center.

Ad Majorem Dei Gloriam

TABLE OF CONTENTS

LIST OF TABLES

LIST OF FIGURES

LIST OF SYMBOLS AND ABBREVIATIONS

S	Seebeck Coefficient [V/K]
TEC	Thermoelectric Cooler
F-TEC	Fin Thermoelectric Cooler
COP	Coefficient of Performance
TE	Thermoelectric
q_c''	Cold Side Heat Flux [W/m^2]
L	TE Leg / Blade Height [m]
h	Convective Heat Transfer Coefficient [W/m^{2}K]
TEG	Thermoelectric Generator
Q_c	Cold Side Heat [W]
P	Power [W]
zT	Material Figure-of-Merit
σ	Electrical Conductivity [S/m]
k	Thermal Conductivity [W/mK]
T	Absolute Temperature [K]
ZT	Module Figure-of-Merit
S_{mod}	Module Seebeck Coefficient [V/K]
R_{eff}	Module Electrical Resistance [Ω]
K_{mod}	Module Thermal Conductance [W/K]
T_h	Hot Side Junction Temperature [K]
T_c	Cold Side Junction Temperature [K]
J	Electrical Current [A]

Ac	Leg / Blade Cross-sectional Area [m^2]
R	Electrical Resistance [Ω]
ζ	Simplifying Grouping of Terms - JR_{eff}/S_{mod} [K]
Z	Z in Module Figure-of-Merit, ZT [K^{-1}]
k_n	Thermal Conductivity of N-type Leg [W/mK]
k_p	Thermal Conductivity of P-type Leg [W/mK]
σ_n	Electrical Conductivity of N-type Leg [S/m]
σ_p	Electrical Conductivity of P-type Leg [S/m]
PF	Power Factor [W/K^2m]
k_B	Boltzmann Constant [m^2kg/s^2K]
e	Carrier Unit Charge [C]
$\bar{h}$	Planck's Constant [Js]
m^*	Effective Mass [kg]
π	Pi
n	Carrier Concentration [m^{-3}]
u	Electron Mobility [m^2/Vs]
τ_m	Relaxation Time [s]
k_e	Electron Thermal Conductivity [W/mK]
L_n	Lorenz Number [$W\Omega/m^2$]
k_l	Lattice Thermal Conductivity [W/mK]
C_v	Volumetric Specific Heat [J/kgK]
υ_s	Sound Velocity [m/s]
λ_{ph}	Phonon Mean Free Path [m]
1D	One Dimensional

2D	Two Dimensional
CSHX	Cold Side Heat Exchanger
3D	Three Dimensional
L_{ins}	Thermoelectric Blade Insulation Length [m]
w	Half-width of Thermoelectric Blade [m]
j	Current Density [A/m^2]
t	Half-thickness of Thermoelectric Blade [m]
FF	Fill Factor
Bi_t	Biot Number
L_c	Characteristic Length [m]
q_x	Taylor Expansion Heat Flow – at x [W]
q_{x+dx}	Taylor Expansion Heat Flow – at x + dx [W]
dq_{conv}	Convective Heat Transfer Rate [W]
A_s	Surface Area [m^2]
T_{inf}	Ambient Temperature [K]
p	Perimeter [m]
Q_{Joule}	Heat Generation due to Joule Heating [W]
T_1	Temperature of Section 1 [K]
T_2	Temperature of Section 2 [K]
$\dot{g}'$	Heat Generation Rate per Unit Length [m]
P	Electrical Resistivity [Ωm]
θ_1	Temperature Change of Variable for Section 1 [K]
E_{in}	Energy In [W]
E_{out}	Energy Out [W]
E_{gen}	Energy Generation [W/m^3]

q''_{cond} Conduction Heat Flux [W/m^2]

q''_{conv} Convective Heat Flux [W/m^2]

$q_{pel,CS}$ Cold Side Peltier Effect [W]

$q_{Pel,HS}$ Hot Side Peltier Effect [W]

q''_{tip} Tip Heat Flux [W/m^2]

θ_2 Temperature Change of Variable for Section 2 [K]

C_1 Constant of Integration 1

C_2 Constant of Integration 2

C_3 Constant of Integration 3

C_4 Constant of Integration 4

R Cumulative Thermal Resistance [K/W]

R_{CS} Cold Side Heat Exchanger Thermal Resistance [K/W]

R_{ins} Refrigerated Space Insulation Normalized Thermal Resistance [K/W]

R_{ref} Refrigerated Space Insulation Thermal Resistance [K/W]

N Number of Thermoelectric Blades

θ Temperature Change of Variable for Uninsulated F-TEC[K]

C_5 Constant of Integration 5

C_6 Constant of Integration 6

A Simplifying Grouping of Terms – A

B Simplifying Grouping of Terms – B

D Simplifying Grouping of Terms – C

E Simplifying Grouping of Terms – D

F Simplifying Grouping of Terms – E

G Simplifying Grouping of Terms – G

$q''_{c,U}$ Cold Side Heat Flux for Uninsulated Fin Thermoelectric Cooler [W/m^2]

$q''_{c,max}$	Max Cold Side Heat Flux for Fin Thermoelectric Cooler [W/m^2]
$L_{ins,opt}$	Optimum Insulation Length as L Approaches Infinity [m]
$L_{ins,optL}$	Optimum Insulation Length when L is Less Than Optimum [m]
$L_{ins,max}$	Insulation Length as R Approaches Infinity [m]
$q''_{c,U,max}$	Maximum Uninsulated Cold Side Heat Flux [W/m^2]
χ	Desired Fraction of $q''_{c,U}$: $0 < \chi < 1$
L^*	Optimum Blade Length [m]
τ_1	Simplifying Grouping of Terms
τ_2	Simplifying Grouping of Terms
L_0	Blade Length at which q''_c is 0 [m]
A_{mod}	Module Area [m^2]
$q''_{c,mod}$	Module Cold Side Heat Flux [W/m^2]
s	Fin Spacing [m]
u_0	Upstream Air Velocity [m/s]
u_f	Fin Air Velocity [m/s]
Nu	Nusselt Number
Pr	Prandtl Number
k_{air}	Thermal Conductivity of Air [W/m^2]
I_T	Thermal Insulance [Km^2/W]
$Q_{c,mod}$	Module Heat Flow [W]
ρ_{air}	Density of Air [kg/m^3]
μ_{air}	Viscosity of Air [Ns/m^2]

SUMMARY

Thermoelectric coolers (TECs) are attractive cooling devices because they have no moving parts and operate without the use of global warming potential (GWP) refrigerants. However, due to a low coefficient of performance (*COP*) and high system costs, TECs are limited to niche applications such as wine coolers, medical refrigerators, and luxury car seats where cost and efficiency are insensitive. Most thermoelectric (TE) research has been focused on improving TE material properties while neglecting the impact of device architecture on performance. However, recent research indicates that device architecture plays a significant role in device performance. Herein, the extent to which device architecture can improve performance is investigated, specifically via the integration of the thermoelectric elements into the heat exchanger.

By shaping the TE material into a blade, the portion of the TEC leg above ambient temperature can function as a heat exchanger fin, effectively eliminating one of the most expensive parts of a TEC module. Further, insulation enclosing the outer surface of the fin that is below ambient temperature inhibits inadvertently absorbing heat from the environment and maximizes the cold side heat flux (q_c''). Key questions that are investigated are the impact of enabling convection off the surface of a TE blade, the effect of current density, and the effect of device geometry (*i.e.*, fin length, width, and insulation length) on q_c'' and *COP*. It is demonstrated that q_c'' converges to a maximum as fin length (L) increases, representing a departure from conventional flat-plate TECs. Further, by enabling convective heat transfer from the TE fin, only Joule heating and conduction heat transfer in the insulated region detracts from q_c''. Finally, a design strategy consisting of

numerous closed-form expressions that identify key geometric dimensions that maximize q_c'' is developed.

CHAPTER 1. INTRODUCTION

1.1 Introduction to Thermoelectric Effects

Thermoelectric coolers (TECs) are solid-state devices that utilize the Peltier effect to produce cooling.[1] The Peltier effect is one of three thermoelectric effects: the Peltier effect, Seebeck effect, and Thompson effect.[2] The Peltier effect describes the flow of electric current across dissimilar materials resulting in heat being absorbed or liberated at the junctions of the materials. As current flows, the temperature of one junction, the hot junction (T_h), increases, and the other, the cold junction (T_c), decreases. The absorption or liberation of heat is due to conducting electrons transferring heat energy from the cold junction to the hot junction. The amount of heat energy absorbed or released is directly related to the difference between the electrochemical potentials of the TE materials forming the junction. The Peltier and Seebeck effects are the result of the same fundamental phenomenon. The Seebeck effect describes the generation of a voltage due to a temperature difference across the material. TECs utilize the Peltier effect and thermoelectric generators (TEGs) utilize the Seebeck effect.[1]

1.2 Quantification of Thermoelectric Cooler Performance

1.2.1 Performance Quantification

The Coefficient of Performance (*COP)* is a metric used to quantify the amount of cooling (Q_c) provided by a given power (P) input; $COP = \frac{Q_c}{P}$. The *COP* and cold side heat flux (q_c'') of TECs are directly related to the material dimensionless figure-of-merit:

$zT = \frac{S^2\sigma}{k}T$, where S is the Seebeck coefficient, σ is the electrical conductivity, k is the thermal conductivity, and T is the absolute temperature.[2] TE modules traditionally consist of p- and n-type semiconductor legs, connected electrically in series and thermally in parallel between two thin ceramic plates. For a module, the module figure-of-merit (ZT) is defined as: $ZT = \frac{S_{mod}^{\ 2}}{R_{eff}K_{mod}}T$, where S_{mod} is the module Seebeck coefficient, R_{eff} is the electrical resistance of the module, and K_{eff} is the thermal conductance across the module. A two-leg module consisting of a p- and an n- type leg is mounted between two heat exchangers is depicted below in **Fig. 1**.

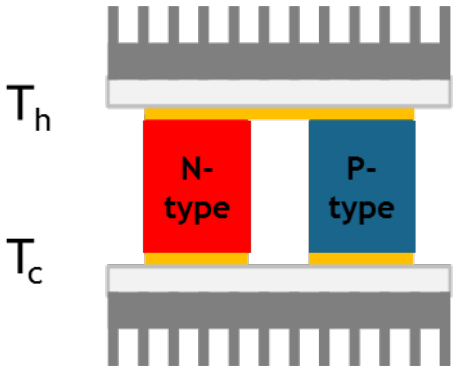

Figure 1 – Two leg TE module. T_h is the hot side junction temperature and T_c is the cold side junction temperature.[3]

The analysis of a two-leg TEC module begins with the following general simplifying assumptions: (*i*) there is no heat transfer from the hot side to the cold side of the device except through the TE legs, (*ii*) the electrical contact resistance at the junctions is negligible, (*iii*) the legs have constant cross-sectional area, (*iv*) the electrical conductivity (σ), thermal conductivity (k), and Seebeck coefficient (S), are temperature independent, and (*v*) the thermal contact resistance of the junctions and heat exchangers is negligible[2].

The cold side heat flow (Q_c) can be evaluated by applying a control volume energy balance on the control volume around the cold junction to yield:[2]

$$Q_c = S_{mod} J T_c - \tfrac{1}{2} J^2 R_{eff} - K_{mod}\left(T_h - T_c\right) \tag{1}$$

where J is the current, $S_{mod} = |S_n| + |S_p|$, $R_{eff} = A_p/L\sigma_p + A_n/L\sigma_n$, where p and n signify semiconductor types, $K_{mod} = k_p A_p/L + k_n A_n/L$, A_p and A_n are the cross-sectional areas of the legs, and L is the TE leg height. The power input, P, is composed of the Joule heating due to the material resistance, and the additional power necessary to overcome the voltage generated by the Seebeck effect:[2]

$$P = J^2 R_{eff} + S_{mod} J \Delta T\,, \tag{2}$$

in Watts, where $\Delta T = \left(T_h - T_c\right)$. The flat-plate TEC *COP* is defined as:

$$COP = \frac{S_{mod} J T_c - \tfrac{1}{2} J^2 R_{eff} - K_{mod}\Delta T}{S_{mod} J \Delta T + J^2 R_{eff}}. \tag{3}$$

Defining a new grouping of terms, $\zeta = JR_{eff}/S_{mod}$, **Eqn. 3** becomes:

$$COP = \frac{\zeta T_c - \tfrac{1}{2}\zeta^2 - \Delta T/Z}{\zeta \Delta T + \zeta^2}, \tag{4}$$

where Z is defined as[2]:

$$Z = \frac{S_{pn}^{\ 2}}{\left[\left(\frac{k_n}{\sigma_n}\right)^{1/2} + \left(\frac{k_p}{\sigma_p}\right)^{1/2}\right]^2}. \quad (5)$$

For a single-leg module (either p- or n-type), multiplying both sides by T and only considering the contribution of the single leg, simplifies **Eqn. 5** to zT. **Equation 4** demonstrates that improvements in zT directly increase COP. Therefore, materials with a combination of high σ, high S, and low k perform the best as TE materials. Doped bismuth telluride is the most commercially viable TE material available, with a $zT \sim 1$ at room temperature.

1.3 Research Initiatives Focused on High zT

As a consequence of **Eqn. 4**, the majority of TE research has been focused on developing high zT materials. A material consisting of a large power factor, ($PF = S^2\sigma$), and low k are necessary for high zT. Unfortunately, the thermoelectric properties that zT is composed of is often anti-correlated[1] making improvements to zT difficult. The Seebeck coefficient is indirectly related to the carrier concentration of a material. A high Seebeck coefficient is characteristic of low carrier concentration materials and a low Seebeck coefficient is characteristic of high carrier concentration materials. The relationship between the Seebeck coefficient and carrier concentration for degenerate semi-conductors is determined by:[1, 4, 5]

$$S = \frac{8\pi^2 k_B^2}{3e\bar{h}^2} m^* T \left(\frac{\pi}{3n}\right)^{2/3}, \quad (6)$$

where k_B is the Boltzmann constant, e is the carrier charge, $\bar{h}$ is Planck's constant, m^* is the effective mass of the charge carrier, and n is the carrier concentration. The electrical conductivity is related to carrier concentration by:[1, 4, 5]

$$\sigma = neu = ne^2\tau_m / m, \quad (7)$$

where u is the electron mobility, τ_m is the relaxation time, and m is the mass of the charge carrier. By doping, n can be altered in a material; however, as **Eqns. 6** and **7** demonstrate, S is indirectly related to n, and σ is directly related to n. The anti-correlated relationship of S and σ on carrier concentration results in an optimum carrier concentration that maximizes the PF, which can be achieved by varying the doping level.[1] The thermal conductivity is related to the carrier concentration, but to a lesser degree since most semiconductors are dominated by the lattice contribution to thermal conductivity[1], therefore making the PF optimization by doping a useful and well established means of maximizing zT.

The TE material thermal conductivity is composed of an electronic contribution (k_e) and a lattice contribution (k_l). k_e is the result of charge carriers transporting heat through the crystal lattice, k_l is the result of phonons transporting heat through the lattice.[1, 4, 5] The k_e is described by the Wiedemann-Franz Law, defined as: $k_e = L_n\sigma T$ [1, 4, 5], where L_n is the Lorenz number, thereby proportionally coupling k_e to σ and rendering any change to k_e ineffective at improving zT. The k_l contribution to k is defined as: $k_l = 1/3 C_\upsilon \upsilon_s \lambda_{ph}$, where

C_υ is the specific heat capacity, υ_s is the sound velocity, and λ_{ph} is the mean free path of the phonon.[5] However, k_l is not related to S or σ and therefore is a viable means of reducing the material thermal conductivity.[1, 5]

Research interest post-1990s for TEs has been devoted to developing methods of reducing the lattice thermal conductivity to improve zT.[5, 6] Numerous comprehensive reviews of TE material development are available.[1, 5, 6] The ideal TE material is one that exhibits characteristics of a low (glass-like) thermal conductivity and high (crystal-like) electrical conductivity, termed phonon-glass electron-crystal (PGEC) properties.[1, 4-6] On a bulk material scale, reduced lattice thermal conductivity can be accomplished by (*i*) increasing phonon scattering sites, (*ii*) introducing complex structures that separate the electron-crystal from the phonon-glass, and (*iii*) mixing multiphase composites on low dimensional materials to increase scattering.[6] Common families of bulk PGEC TE materials are skutterudites[1, 5, 6], achieving a zT as high as 1.7 at 850 K[6], clathrates[1, 5, 6], achieving a zT as high as 1.3 at 1000 K[6], half-Heusler compounds[1, 5], achieving a zT as high as 1.5 at 700 K [6], Zintl phases[1, 6], achieving a zT of 1 at 900 K[6], chalcogenides[1, 6] reaching a zT as high as 1.5 at 1000 K[4], and β-Zn_4Sb_3[1, 5, 7] demonstrating a $zT \sim 1.35$ at 400 K.[6, 7] Alternatively, nanostructuring of TE materials takes advantage of quantum and classical size effects to reduce the phononic contribution of thermal conductivity. Commonly investigated nanostructuring techniques utilize quantum wells, superlattices, quantum wires, and quantum dots to improve zT.[1, 5, 6] Due to the effectiveness of blocking phonons on the quantum scale, nanostructuring has been relatively successful. Nanostructured $Bi_2Te_3/Sb_2/Te_3$ has achieved a zT of 2.4 at 300K[5, 6, 8] and p-type PbTe boasts a zT of 1.5

at 773 K.[6, 9] Aside from nanostructured or complex crystal materials, SnSe, a rock-salt structure, has demonstrated a *zT* of ~ 2.6.[10]

Despite the advances in *zT*, manufacturing nanostructured and complex crystal lattice materials into bulk TE materials is challenging and expensive. Additionally, there is often a large discrepancy between theoretical performance derived utilizing *zT* and the actual performance of the module based on *ZT*. The difference is the result of parasitic losses, such as electrical interconnect resistance and thermal interface resistance[11], and the temperature dependence of the TE properties[1], which are difficult to overcome.

By reconsidering the flat-plate TE module design and the simplifying assumptions the model is based upon, other opportunities to improve performance have been identified. For instance, Itoigawa re-evaluated TE leg geometry and introduced corrugated leg thin-film TECs that take advantage of flexible film printing techniques and boast a comparable *COP* to its conventional flat-plate counterpart.[12, 13] Menon developed a radial TEG architecture that reduces the module thermal conductance and boasts a 6-fold increase in power density compared to its flat-plate counterpart.[3] Furthermore, Fabian demonstrated that utilizing tapered legs, rather than uniform cross-sectional area legs in a flat-plate TEG module, yields an increase in *ZT* of 87% compared to that of a similar flat-plate module and an effective *zT* increase of 29%.[11] Additionally, by considering TEs from a cost perspective, it has been demonstrated that over a large class of TE materials and applications, the dominant cost of TEG systems (applicable to TECs as well) is the heat exchangers, not the TE material.[14]

1.4 New Direction in Thermoelectric Module Architecture / Objective

It can be concluded from the literature review, that the major focus of research has been on improving material properties, with less attention paid to the impact of device architecture on device performance, or to reducing the main cost drivers that limit wide scale adoption of TECs. However, research clearly indicates that device architecture plays a significant role in performance.[3, 11, 12] This work shifts attention away from material property improvements and focuses on investigating the TEC system holistically (*i.e.* TE material, TE material geometry, electrical and thermal interconnects, and heat exchangers) to devise architecturally based thermal management strategies that improve overall device performance and reduce module cost. By shaping the TE material into a blade, the portion of the TEC leg above ambient temperature can function as a heat exchanger fin, effectively eliminating one of the most expensive parts of a TEC system – the heat exchanger. Furthermore, on the portion of the fin below ambient temperature, insulation can enclose the outer surface of the fin to prevent heat from being absorbed from the surroundings into the TE blade. The aim of this work is to establish the impact of fin-thermoelectric cooler (F-TEC) architecture supplemented with cold side insulation on TEC device performance (*i.e.*, q_c'' and *COP*.)

1.5 Thesis Outline

This thesis consists of five chapters laid out as follows:

Chapter 1 provides an introduction to TEs, highlights past TE research directions, and identifies device architectural strategies that could improve device q_c'' and *COP*.

Chapter 2 provides an introduction to F-TECs, followed by a brief description of the 1D heat transfer models and relevant analytical expressions that describe the system, and lastly the method that will be used to optimize *COP* and q_c''.

Chapter 3 optimizes the geometry and current density of a F-TEC to maximize q_c'' and *COP* and discusses key performance characteristics of F-TECs. The impact of the convective heat transfer coefficient on q_c'' is additionally demonstrated. Chapter 3 concludes by comparing the performance of F-TECs to conventional flat-plate TECs.

Chapter 4 utilizes a COMSOL model of the F-TEC to validate the 1D model under two circumstances. First, by assuming a constant convective heat transfer coefficient across the surface of the fin, and second by enabling convection via air flow over the F-TEC module.

Chapter 5 discusses concluding remarks and future work.

CHAPTER 2. F-TEC MODELING

2.1 F-TEC Module Overview

A F-TEC module is composed of p- and n-type TE blades connected electrically in series, as depicted in **Fig. 2**. The portion of each blade where the surface temperature exceeds ambient temperature, termed the fin hot side, is exposed to forced air which enables convective cooling of the fin hot side. The portion of each blade where the surface temperature is below the ambient temperature, referred to as the fin cold side, is insulated to limit heat transfer from the surroundings into the TE blades. The TE blades are mounted to a cold side heat exchanger (*e.g.*, cold plate), and careful thermal design of the entire system can maximize the cold side heat flux q_c'', and the cooler's *COP*.

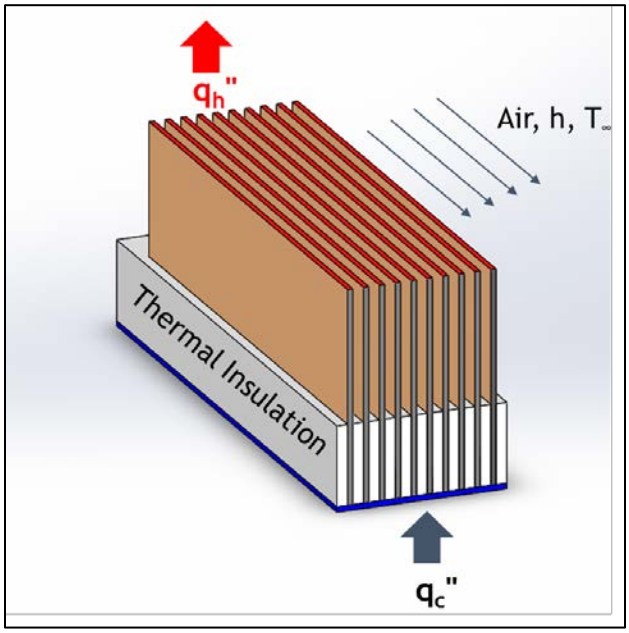

Figure 2 – Cross-sectional schematic of a F-TEC module. TE material is shaped into p- and n-type blades and assembled into a TE fin module. Convection along the TE fin hot side serves as an integrated heat exchanger. (The electrical connections between individual blades are not depicted for simplicity.)

2.2 Modeling Strategy

First, one-dimensional (1D) heat transfer models of the uninsulated and insulated F-TECs are presented. The 1D insulated F-TEC model evaluates the impact on device performance of the fin architecture supplemented with thermal insulation. Closed-form expressions for critical geometric design parameters (*e.g.* fin length), are derived using the uninsulated model. Performance similarities between the insulated and uninsulated F-TECs result in new analytical expressions that describe the device physics of insulated and uninsulated F-TECs. General solutions and cooler specific solutions are then derived for both the insulated and uninsulated F-TECs. The F-TEC's performance is then evaluated and compared to conventional flat-plate TEC performance and reported in the Key Findings section. Finally, a COMSOL model is utilized to validate the 1D fin model.

The F-TEC results herein are utilized to quantify device performance improvements relevant to many device applications, such as a refrigerator or car air conditioner. Careful attention is paid to not impose any unnatural conditions upon the general solutions and conversely, to remain sufficiently detached from a particular TEC application, which makes these results widely applicable. Therefore, rather than imposing an arbitrary cold side temperature on the general solution, only a cold side heat exchanger (CSHX) is applied to the blade. Furthermore, a cold side heat exchanger is present in every application and can be as simple as a plate. The thermal resistance of the CSHX scales with the cross-sectional area of the module, and enables the analysis to elucidate application relevant device performance without being overly application specific.

Figure 3 illustrates a cross-sectional view of a single F-TEC blade in three dimensions (3D) with the relevant geometry and coordinate system.

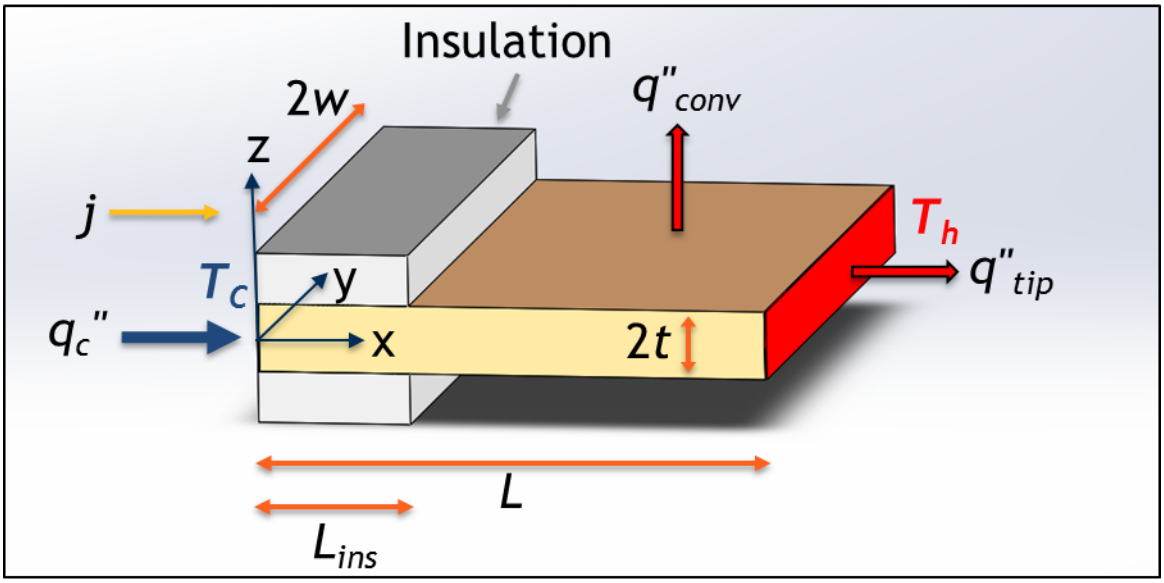

Figure 3 – 3D depiction of a F-TEC blade where L_{ins} is the insulation length, L is the fin length, 2w is the fin width, 2t is the fin thickness, and j is the current density. The hot and cold side junction temperatures are labeled T_h and T_c, respectively.

q_c'' and *COP* can be optimized by modifying the geometry (*i.e.*, insulation length (L_{ins}), fin length (L), and fin width(w)) and operating parameters (*i.e.* current density ($j=J/A_c$)). The existence of an optimum aspect ratio between the height and cross-sectional area (A_c) of a thermoelectric leg on Q_c is well established in literature.[15] The competing trends between Joule heating and conduction as a function of the aspect ratio are demonstrated in **Eqn. 1** and necessitate the existence of an optimum aspect ratio. Heat exchanger fins are designed to be sufficiently thin in order to maximize surface area for convection, therefore t is constrained as will be discussed further in **Section 2.6.1**. If an optimum aspect ratio exists for F-TECs, varying the width of the fin while holding the thickness constant will maintain the optimum aspect ratio that maximizes Q_c or *COP*.

For simplicity, the TE properties of the p- and n-type blades are considered to be equal in magnitude but have Seebeck coefficients that are opposite in sign, therefore eliminating the need for any geometry matching condition and achieving identical performance between semiconductor types. Without this simplification, the conventional geometry matching condition for flat-plates can be used to vary the cross-sectional area and leg length of p-type and n-type blades to be appropriately matched. The Fill Factor (*FF*) selected for a F-TEC is dependent upon the desired width of the fin and, as a result, is application specific. Therefore, the F-TEC analysis herein considers the performance (q_c'' and *COP*) for an individual p-type TE leg, except for the performance comparison of the F-TEC to a conventional flat-plate TEC, which considers a two blade F-TEC and a flat-plate TEC with equal volume of material. This allows the performance of TE blades to be evaluated without convoluting the *FF* into the F-TEC performance.

2.3 Conventional Fin Heat Transfer Model

Multi-dimensional heat transfer consisting of conduction, convection, internal heat generation, and boundary heat generation is complex to solve analytically. Efficacious simplifications and approximations can distill the solution down into a more useful form. The conventional treatment of heat transfer in extended surfaces (*i.e.* fins) reduces the number of necessary spatial dimensions to one. Therefore, before introducing the F-TEC models, the conventional heat transfer analysis of a fin is demonstrated as background for the modeling approach utilized for F-TECs.

A fin is an extended surface that improves heat transfer from a solid to a fluid. **Figure 4** depicts a basic fin adopted from Bergman *et al.*[16] Fins analyses are commonly simplified

by treating the heat transfer as occurring in quasi 1D. Quasi 1D heat transfer can account for heat transfer in multiple directions, but the temperature in the solid only varies in one direction. The Biot number (Bi_t) is a useful dimensionless parameter that quantifies when this simplification is acceptable. The Biot number, defined as hL_c/k, where h is the convective heat transfer coefficient of the fluid and L_c is the characteristic length, is the ratio of convective to conductive resistances. When the Biot number is sufficiently small, less than 0.1, external convective resistance is greater than internal conductive resistance and therefore there is appreciable temperature variation only along the length of the fin.

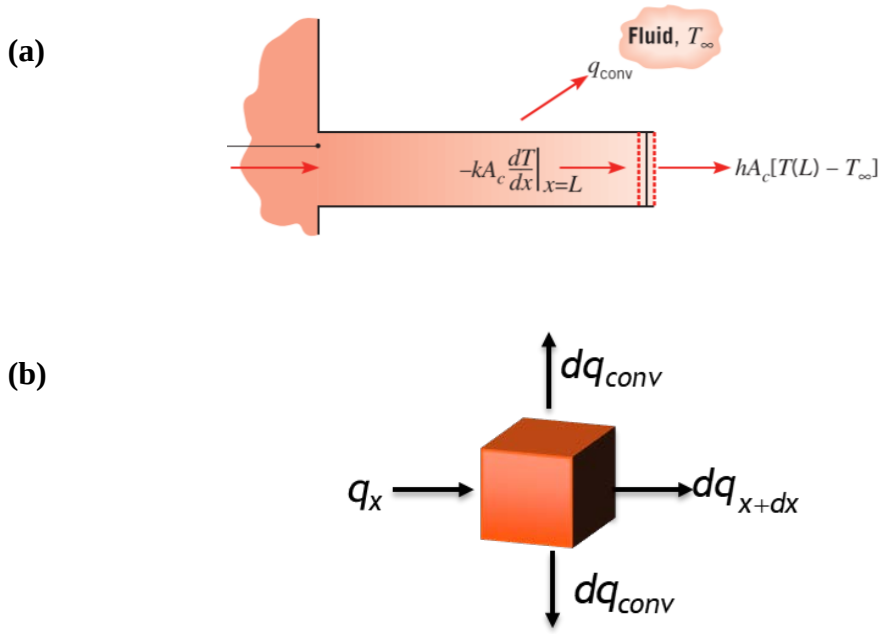

Figure 4 – (a) Heat transfer in an extended surface fin[16] and (b) the corresponding differential element.

The basic assumptions applied to analyze the heat transfer in a rectangular fin are: (*i*) the Biot number is sufficiently small (*i.e.* much less than unity), (*ii*) the temperature variation varies in 1D, (*iii*) the system is at steady-state, (*iv*) the thermal conductivity (k) is isotropic and spatially constant, (*v*) the convective heat transfer coefficient (h) is constant and

uniform across the surface of the fin, (*vi*) radiative exchange with the surface of the fin is negligible, (*vii*) there is no heat generation within the fin. An energy balance is then performed on a differential element of the fin depicted in **Fig. 4**, and the governing heat transfer equation is derived.

The energy balance is:

$$q_x - q_{x+dx} - dq_{conv} = 0, \tag{8}$$

where q_x, q_{x+dx}, and dq_{conv} are the Taylor expansion approximations. Substituting and differentiating yields:

$$\frac{d^2T}{dx^2} + \frac{1}{A_c}\frac{dA_c}{dx}\frac{dT}{dx} - \frac{h}{k}\frac{dA_s}{dx}\left(T - T_\infty\right) = 0, \tag{9}$$

where A_s is the surface area of the fin and T_∞ is the ambient temperature. In the case of a rectangular fin, $\frac{dA_c}{dx} = 0$ and $A_s = px$, where p is the perimeter of the fin in the $y-z$ plane. Further simplification yields the governing equation in the form of a non-homogenous second order ordinary differential equation:

$$\frac{d^2T}{dx^2} - \frac{hp}{kA_c}\left(T - T_\infty\right) = 0, \tag{10}$$

the solution of which can be readily obtained by integration subject to the appropriate boundary conditions.

2.4 Derivation of 1D Insulated F-TEC Model

The 1D insulated F-TEC will utilize many of the same assumptions and simplifications utilized in the conventional fin heat transfer analysis. The following simplifying assumptions are made: (*i*) the Biot number (where $L_c = t$) is sufficiently small (*i.e.*, much less than unity), (*ii*) the temperature varies in 1D, (*iii*) the system is at steady-state, (*iv*) the thermal conductivity (k) is isotropic and spatially constant, (*v*) the convective heat transfer coefficient (h) is spatially constant across the surface of the fin, (*vi*) that radiative exchange with the surface of the fin is negligible, (*vii*) the thermal insulation is adiabatic, (*viii*) the material is isotropic and (*ix*) the material properties are temperature independent (Thompson effect is negligible). A 1D schematic of the insulated F-TEC considering the effect of conduction, convection (q''_{fin} and q''_{tip}), uniform Joule heating (Q_{Joule}), and the Peltier effect at both junctions ($q''_{Pel,CS}$ and $q''_{Pel,HS}$) is depicted in **Fig. 5.**

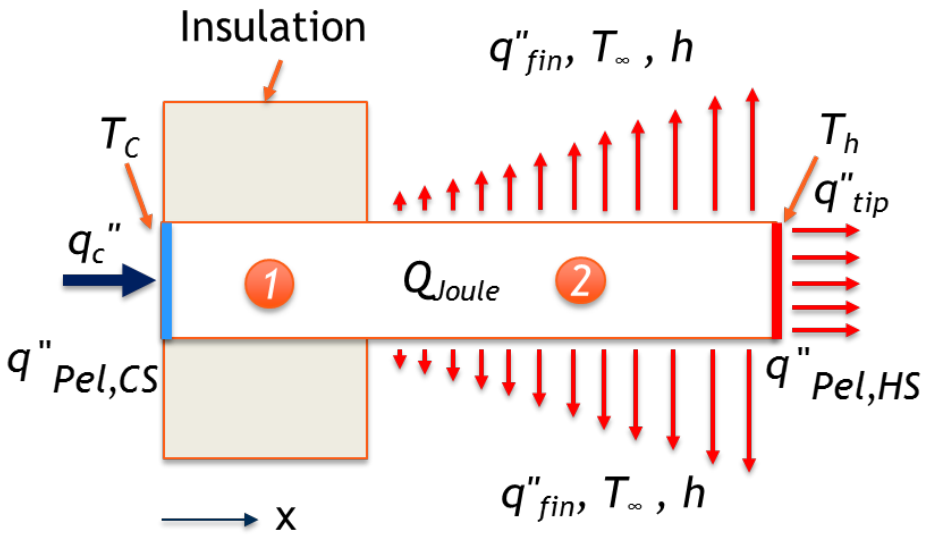

Figure 5 – 1D (*x*-*z* plane) heat transfer diagram of an insulated TE fin.

2.4.1 General Solution

The fin is first separated into two coupled sections (labelled section 1 and section 2 in **Fig. 5**), to develop the governing heat transfer equations. T_1 and T_2 designate the temperature profiles in section 1 and section 2, respectively. Beginning with section 1, an energy balance is completed on the differential element depicted in **Fig. 6.** The energy balance is similar to **Eqn. 8** with the addition of heat generation and the exclusion of convection due to the insulation.

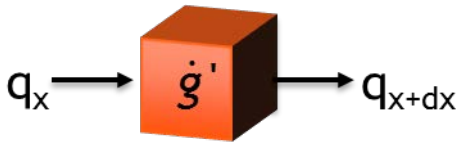

Figure 6 – Heat transfer energy balance on a 1D differential element in the insulated region (section 1) of the insulated F-TEC.

The energy balance is:

$$q_x + \dot{g}'dx - q_{x+dx} = 0\,, \tag{11}$$

where $\dot{g}'$, is the heat generation rate per unit length:

$$\dot{g}' = j^2 A_c \rho\,, \tag{12}$$

where j is the magnitude of the current density and ρ is the resistivity. Substituting the Taylor expansion approximations for q_x and q_{x+dx} and **Eqn. 12** into **Eqn. 11**, and applying the familiar change of variable ($\theta_1 = T_1 - T_\infty$) yields the Section 1 governing equation:

$$\frac{d^2\theta_1}{dx^2} = -\frac{j^2\rho}{k}. \tag{13}$$

For section 2 the differential element is depicted as:

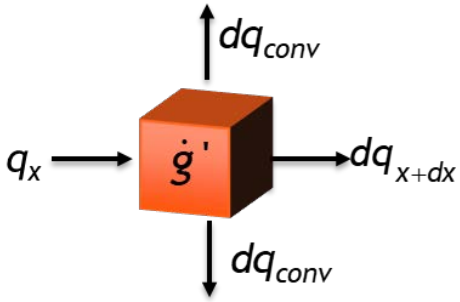

Figure 7 – Heat transfer energy balance on a 1D differential element in the section 2 region (region of the fin exposed to convection) of the insulated F-TEC.

The corresponding energy balance is:

$$q_x + \dot{g}'dx - q_{x+dx} - dq_{conv} = 0. \tag{14}$$

Utilizing the same simplifications applied to **Eqn. 8,** and **Eqn. 12** yields:

$$j^2\rho A_c + kA_c\frac{d^2T_2}{dx^2} - h\frac{dA_s}{dx}\left(T_2 - T_\infty\right) = 0, \tag{15}$$

where $dA_s/dx = p$ and $p = 2\left(2w + 2t\right)$. However, by definition of a blade, $2t << 2w$ and L therefore p can be approximated as $4w$. Substituting p, $A_c = 4wt$, and $\theta_2 = T_2 - T_\infty$ into **Eqn. 15** simplifies the Section 2 governing equation to:

$$\frac{d^2\theta_2}{dx^2} - \frac{h}{kt}\theta_2 + \frac{j^2\rho}{k} = 0. \tag{16}$$

The boundary conditions of the F-TEC are derived by performing energy balances on the left and right faces. The left boundary experiences conduction, a heat flux, and a heat sink (due to the Peltier effect.) An energy balance on the left face yields:

$$E_{in} - E_{out} + E_{gen} = 0,$$

or
$$q''_{cond} - q''_c + q''_{Pel,CS} = 0. \tag{17}$$

The individual terms are:

$$q''_{cond} = -k\left.\frac{dT_1}{dx}\right|_{x=0}, \tag{18}$$

and
$$q''_{Pel,CS} = -jS\,T_1\big|_{x=0}. \tag{19}$$

After substitution yields:

$$q_c'' + k\left.\frac{dT_1}{dx}\right|_{x=0} - SjT_1\big|_{x=0} = 0. \tag{20}$$

Lastly, applying the change of variables, $\theta_1 = T_1 - T_\infty$, and rearranging provides the cold side boundary condition:

$$-k\left.\frac{d\theta_1}{dx}\right|_{x=0} + Sj\left(\theta_1\big|_{x=0} + T_\infty\right) = q''_c \tag{21}$$

The hot side boundary experiences conduction, a heat flux, and a heat source (due to the Peltier effect.) The energy balance yields:

$$q''_{cond} - q''_{tip} + q''_{Pel,HS} = 0, \tag{22}$$

where the individual terms are:

$$q''_{cond} = -k\left.\frac{dT_2}{dx}\right|_{x=L}, \tag{23}$$

and

$$q''_{Pel,HS} = jS\,T_2\big|_{x=L}\ . \tag{24}$$

Combining these equations yields:

$$-k\left.\frac{dT_2}{dx}\right|_{x=L} + Sj\,T_2\big|_{x=L} = q''_{tip}\,. \tag{25}$$

In addition, the convective heat transfer off the tip is modelled as:

$$q''_{tip} = \frac{h}{k}\left(T_2\big|_{x=L} - T_\infty\right). \tag{26}$$

Applying **Eqn. 26** and the change of variable: $\theta_2 = T_2 - T_\infty$ yields the boundary condition:

$$-k\left.\frac{d\theta_2}{dx}\right|_{x=L}+\theta_2\big|_{x=L}\left(Sj-h\right)+SjT_\infty=0\,. \tag{27}$$

The additional two equations necessary to satisfy the number of knowns and unknowns are derived from the interface conditions. At the interface between sections 1 and 2, the heat fluxes are equal, and the temperatures are equal:

$$\begin{aligned} &\text{at } x=L_{ins}, \qquad k\frac{d\theta_1}{dx}=k\frac{d\theta_2}{dx}, \\ &\text{at } x=L_{ins}, \qquad \theta_1=\theta_2\ . \end{aligned} \tag{28}$$

The governing equations, **Eqs. 13** and **16**, are second order non-homogenous ordinary differential equations that can be readily solved. The corresponding temperature profiles are:

$$\theta_1=-\frac{j^2\rho}{2k}x^2+C_1x+C_2\,, \tag{29}$$

and

$$\theta_2=C_3\exp\left(x\sqrt{h/kt}\right)+C_4\exp\left(-x\sqrt{h/kt}\right)+\frac{j^2\rho t}{h}\,. \tag{30}$$

The coefficients of the temperature profile are readily obtained by applying the boundary conditions and interface conditions, **Eqns. 21, 27, and 28**.

2.4.2 Thermoelectric Cooler Solution

The thermal circuit through the cold side heat exchanger to ambient temperature is modelled as:

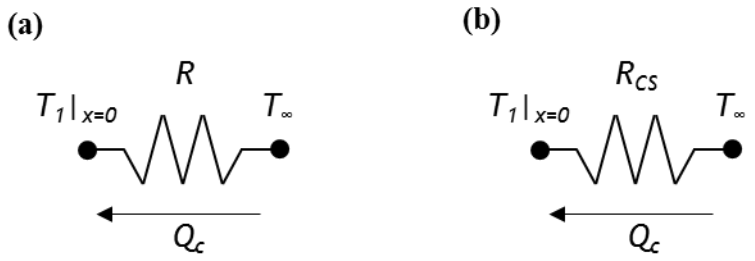

Figure 8 – Thermal circuit analysis of (a) a refrigerated space and (b) only a cold side heat exchanger (CSHX), where *R* and R_{cs} are the thermal resistances of the respective cases in units of K/W.

Applying Fourier's Law to **Figure 8 (a)** and substituting θ_1 in yields:

$$q_c''\big|_{x=0} = \frac{-\theta_1\big|_{x=0}}{A_c R}, \tag{31}$$

where $R = R_{ins} + R_{cs}$ and R_{ins} is the thermal resistance of the refrigerated space insulation (R_{ref}) normalized to the number of legs. R_{ins} can be expressed as $R_{ref}/2N$ where N is the number of blade couples. R_{cs} is the thermal resistance of the CSHX, both R_{cs} and A_c are known. In the case of a F-TEC operating with only a CSHX, R simplifies to R_{cs}. **Equations 21, 27, 29, 30,** and **31** are readily solved simultaneously for the temperature profile coefficients and q_c''.

By evaluating **Eqn. 31** at $x = 0$, the equation simplifies to:

$$q_c''\big|_{x=0} = \frac{-C_2}{A_c R}. \tag{32}$$

The power (P) required to operate the TEC is defined as:

$$P = j^2 \rho A_c L + j A_c S\left(T_h - T_c\right), \tag{33}$$

where the first term is the result of the intrinsic material resistance, and the second term is due to the Seebeck voltage that must be additionally overcome. The *COP* in this model does not consider the power required to operate the heat exchanger fans, as the power consumption is negligible compared to the power of the F-TEC:

$$COP = \frac{Q_c}{P}. \tag{34}$$

where $Q_c = q_c'' A_c$.

2.4.3 Approximate Heat Flux Equation

A simplified equation for q_c'' is derived for the case that the L_{ins} is optimized to maximize q_c''. When L_{ins} is set to the length that maximizes q_c'', a near linear temperature profile develops in section 1. Assuming the temperature profile in section 1 is truly linear and due to geometric symmetry forcing half the Joule heating in section 1 towards the cold side and the other half towards section 2, yields:

$$Q_c = JST_c - \frac{1}{2} J^2 \frac{L_{ins}\rho}{A_c} - \frac{kA_c}{L_{ins}}\left(T_\infty - T_c\right), \tag{35}$$

where T_c is the temperature at $x = 0$. **Equation 35** takes the same form as the equation for the conventional flat-plate TEC's Q_c (**Eqn. 1**) and therefore provides a very useful means of comparing the impact of the F-TEC geometry performance. The CS heat flux for the insulated F-TEC is:

$$q_c'' = jST_c - \frac{1}{2} j^2 L_{ins} \rho - \frac{k}{L_{ins}} \left(T_\infty - T_c \right). \tag{36}$$

When analyzing a system with a CSHX attached (*i.e.* R_{cs} is known) **Eqns. 36** and **31** are combined to yield:

$$q_c'' = \frac{jST_\infty - \frac{1}{2} j^2 L_{ins} \rho}{1 + JSR + \frac{kA_c R}{L_{ins}}}. \tag{37}$$

By combining and simplifying **Eqns. 33**, **34**, and **35** with $J = jA_c$ the *COP* of a F-TEC is:

$$COP = \frac{jST_c - \frac{1}{2} j^2 L_{ins} \rho - \frac{k}{L_{ins}} \left(T_\infty - T_c \right)}{j^2 L \rho + Sj\Delta T},$$

indicating that both F-TEC *COP* and q_c'' (see **Eqn. 36**) are not dependent on the blade cross-sectional area.

2.5 Derivation of 1D Uninsulated F-TEC Model

2.5.1 General Solution

The 1D uninsulated F-TEC model serves as a baseline for F-TEC performance and more importantly is useful in deriving analytical expressions for optimum geometries. A 1D schematic of the uninsulated case is depicted below:

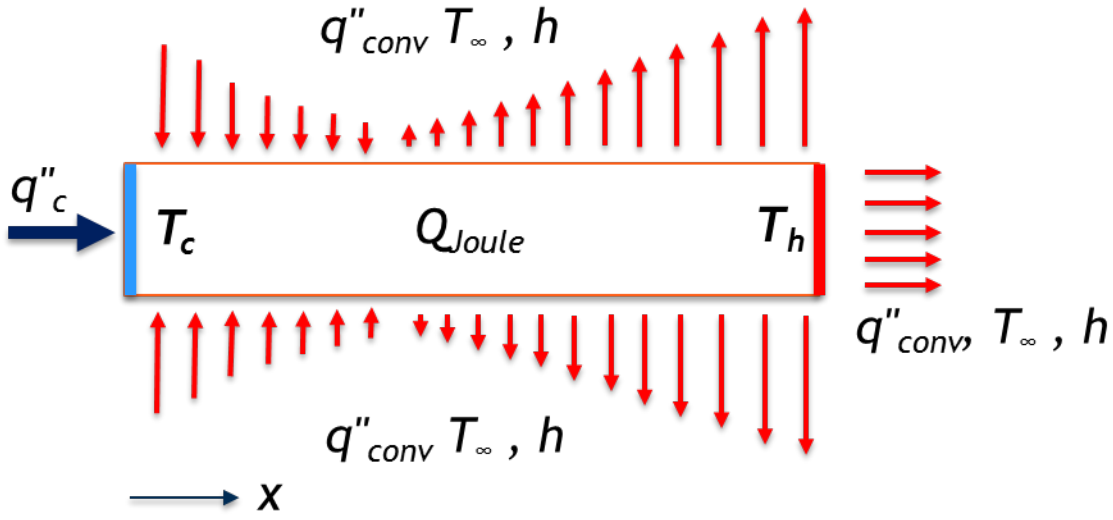

Figure 9 – Schematic of 1D uninsulated F-TEC. Forced air enables convection across the entire surface of the fin. Without insulation the portion of the TE fin below ambient temperature absorbs heat from the environment, therefore decreasing q_c'' and *COP*.

Figure 9 demonstrates that without insulation on the portion of the fin where the temperature is below ambient temperature, q_c'' is reduced because the device absorbs heat from the environment rather than solely through the cold side. In the uninsulated case, $\theta = T - T_\infty$ and the governing equation is derived in the same manner as in the insulated case (**Eqn. 16**):

$$\frac{d^2\theta}{dx^2} - \frac{h}{kt}\theta + \frac{j^2\rho}{k} = 0\,. \tag{38}$$

The boundary conditions at the cold and hot junctions of the fin are developed in the same manner as the insulated F-TEC section 1 cold side boundary condition and the section 2 hot side boundary condition, **Eqns. 21** and **27** respectively:

$$-k\left.\frac{d\theta}{dx}\right|_{x=0} + Sj\left(\theta\big|_{x=0} + T_\infty\right) = q_c'', \tag{39}$$

$$-k\left.\frac{d\theta}{dx}\right|_{x=L} + \theta\big|_{x=L}\left(Sj - h\right) + SjT_\infty = 0. \tag{40}$$

The governing equation (**Eqn. 38**) is readily solved to yield the temperature profile:

$$\theta(x) = C_5 \exp(x\sqrt{h/kt}) + C_6 \exp(-x\sqrt{h/kt}) + \frac{j^2\rho t}{h}. \tag{41}$$

Applying the boundary conditions from **Eqns. 39** and **40** yields:

$$C_5 = \frac{AE - BF\exp\left(-L\sqrt{h/kt}\right)}{DF\exp\left(-L\sqrt{h/kt}\right) - GA\exp\left(L\sqrt{h/kt}\right)}, \tag{42}$$

$$C_6 = \frac{GB\exp\left(L\sqrt{h/kt}\right) - DE}{DF\exp\left(-L\sqrt{h/kt}\right) - AG\exp\left(L\sqrt{h/kt}\right)}, \tag{43}$$

where:

$$A = \sqrt{kh/t} + Sj + \frac{1}{A_c R_{cs}}, \tag{44}$$

$$B = \frac{j^2\rho t}{hA_c R_{cs}} + Sj\left(j^2\rho t/h + T_\infty\right), \tag{45}$$

$$D = Sj - \sqrt{kh/t} + \frac{1}{A_c R_{cs}}, \tag{46}$$

$$E = Sj\left(J^2 \rho t/h + T_\infty \right) - j^2 \rho t, \tag{47}$$

$$F = \sqrt{kh/t} + Sj - h, \tag{48}$$

$$G = Sj - \sqrt{kh/t} - h. \tag{49}$$

2.5.2 Thermoelectric Cooler Solution

The equation for the uninsulated F-TEC heat flux, $q''_{c,U}$ is developed similarly to **Eqn. 31** and is evaluated at $x = 0$, yielding:

$$q''_{c,U} = \frac{-C_5 - C_6 - j^2 \rho t/h}{A_c R_{cs}}. \tag{50}$$

The power consumed, and the corresponding COP of the uninsulated F-TEC are the same as the insulated F-TEC, described by **Eqns. 33** and **34**, respectively.

2.5.3 Optimum Insulation Length

In order to maximize q_c'', at a given L and j, the fin cold side should be insulated up to the point at which the fin reaches T_∞, as will be demonstrated in the Key Findings section. However, it is difficult to derive a useful closed-form solution for the position of T_∞ from the insulated model. Alternatively, a simple closed-form analytical expression for the

position of T_∞ on the uninsulated fin can be readily determined, and due to performance similarities between the two models, it is a useful approximation for the optimum L_{ins} that maximizes q_c'' in the insulated model. Accuracy quantification of the critical dimension approximations compared to solving the full insulated F-TEC equations are presented in Section 3.1.

The maximum heat flux ($q''_{c,max}$) of F-TECs is a function of L_{ins}, L, and j. Holding all other parameters constant, as L approaches infinity, the cold side heat flux converges to a maximum ($q''_{c,max}$). The optimum insulation length ($L_{ins,opt}$) also converges to a maximum that coincides with $q''_{c,max}$. To identify the insulation length that produces the $q''_{c,max}$, the limit of **Eqn. 41** as L approaches infinity is taken with $T = T_\infty$, ($\theta = 0$):

$$0 = \lim_{L\to\infty}\left\{C_5 \exp\left(L_{ins,opt}\sqrt{h/kt}\right) + C_6 \exp\left(-L_{ins,opt}\sqrt{h/kt}\right) + \frac{j^2\rho t}{h}\right\}, \tag{51}$$

which reduces to:

$$0 = \lim_{L\to\infty}\left\{\frac{GB\exp\left(L\sqrt{h/kt}\right) - DE}{DF\exp\left(-L\sqrt{h/kt}\right) - AG\exp\left(L\sqrt{h/kt}\right)}\exp\left(-L_{ins,opt}\sqrt{h/kt}\right)\right\}. \tag{52}$$

An order of magnitude analysis reveals that DE is relatively insignificant, and $DF\exp\left(-L\sqrt{h/kt}\right) \to 0$. By neglecting DE, **Eqn. 51** further simplifies to:

$$L_{ins,opt} = -\sqrt{\frac{kt}{h}} \ln\left(\frac{A}{B}\frac{j^2\rho t}{h}\right). \tag{53}$$

Equation 53 represents the optimum insulation length that maximizes q_c'' when the fin length (L) is sufficiently large. The optimum insulation length that corresponds to a particular L that does not allow q_c'' to converge to a maximum ($L_{ins,optL}$) can be found by an alternative approach. By setting $\theta = 0$, $x = L_{ins,optL}$, with C_5 and C_6 evaluated at L, $L_{ins,optL}$ is solved yielding:

$$L_{ins,optL} = \sqrt{\frac{kt}{h}} \ln\left(\frac{-j^2\rho t/C_5 h \pm \sqrt{\left[j^2\rho t/C_5 h\right]^2 - 4C_6/C_5}}{2}\right), \tag{54}$$

where the real part of $\pm\sqrt{\left[j^2\rho t/C_5 h\right]^2 - 4C_6/C_5}$ is chosen.

2.5.4 Maximum Insulation Length

The insulation length converges to a maximum as the R-value of an insulated space approaches infinity. The maximum insulation length corresponding to a perfectly insulated space is found by taking the limit as R_{cs} approaches infinity:

$$L_{ins,max} = -\sqrt{\frac{kt}{h}} \ln\left(\frac{j^2\rho t}{h}\frac{\sqrt{kh/t} + Sj}{Sj\left(j^2\rho t/h + T_\infty\right)}\right). \tag{55}$$

2.5.5 Expression for Uninsulated F-TEC Maximum Cold Side Heat Flux

The maximum heat flux as a function of L for the uninsulated F-TEC ($q''_{c,U,\max}$) can be evaluated in a similar manner as the optimum insulation length. By taking the limit of **Eqn. 50** as L approaches infinity and holding current density constant, the maximum cold side heat flux for the uninsulated F-TEC is:

$$q''_{c,U,max} = \frac{B/A - m}{A_c R_{cs}}. \tag{56}$$

2.5.6 Optimum Fin Length to Maximize Cold Side Heat Flux

The approximate shortest L, denoted L^*, that corresponds to the maximum heat flux is found by first solving for $q''_{c,U,\max}$. Then $\chi q''_{c,U,\max}$ will be substituted in for q_c'' in **Eqn. 50**. χ is user defined and must be greater than 0 and less than 1. For example, if χ is set to 0.9999, the L^* that corresponds to 99.99% of the $q''_{c,U,\max}$ is then solved for by rearranging **Eqn. 50** to yield:

$$L^* = \sqrt{\frac{kt}{h}} \ln\left(\frac{-\tau_2 \pm \sqrt{\tau_2^{\,2} - 4\left(BG + AG\tau_1\right)\left(-DF\tau_1 - BF\right)}}{2\left(BG + AG\tau_1\right)} \right), \tag{57}$$

where τ_1 and τ_2 equal:

$$\tau_1 = -\chi A_c R_{cs} q''_{c,U,\max} - j^2 \rho t / h, \tag{58}$$

$$\tau_2 = AE - DE \,. \tag{59}$$

2.5.7 Minimum Length Enabling Cooling

The proximity of the hot side relative to the cold side forces the heat flux to be negative until the blade is sufficiently long. The minimum length (L_0) corresponding to the point at which $q_c'' = 0$, is determined by solving **Eqn. 50** with $q_c'' = 0$ for L yielding:

$$L_0 = \sqrt{\frac{kt}{h}} \ln\left(\frac{\tau_2 \pm \sqrt{\tau_2^{\,2} - 4\left({J^2 \rho t}/{h}\; AG - GB \right)\left(BF - {J^2 \rho t}/{h}\; DF \right)}}{2\left({J^2 \rho t}/{h}\; AG - GB \right)} \right) \tag{60}$$

The design strategy describing how to apply the closed-form expressions for critical geometric dimensions is located in Appendix A.1.

2.6 Model Parameters

2.6.1 Fill-Factor and Convective Heat Transfer Coefficient Derivation

In order to determine the required convective heat transfer coefficient (h) the spacing between fins (s), the width of each fin, and the flow characteristics must be known. The spacing between fins is related to the *FF* defined as $FF = {NA_c}/{A_{mod}}$, where N is the number of blades in a module, and A_{mod} is the cross-sectional area of the module. Inducing turbulence would increase the convective heat transfer coefficient and as a result increase q_c''. For a given fan flow rate, turbulence can be induced by three main approaches, (*i*) by increasing the roughness of the fin surface, (*ii*) by spacing the fins out sufficiently far that

the flow eventually becomes turbulent, or (*iii*) by maximizing the velocity between the fins by spacing the fins closer together. For this analysis the blades are assumed to be perfectly smooth, additionally increasing the fin spacing to induce turbulence would negatively impact the *FF* and consequently the module cold side heat flux ($q''_{c,mod}$). However, by spacing the fins closer together turbulence may be induced and the *FF* is maximized to increase $q''_{c,mod}$; therefore the blades are spaced as close together as possible. Due to manufacturing limitations (*e.g.* pick and place machines), conventional flat-plate TE modules leave approximately a 1 mm gap between legs. Assuming similar manufacturing constraints for the F-TEC, the spacing between blades (*s*) will be set to 1 mm to maximize the *FF*. Additionally, on either edge of the module a space of 0.5 mm between the blade and the edge of module is allotted, resulting in a FF of 0.72.

By defining a blade such that $2t << 2w$ and L, the minimum *w* is set as an order of magnitude larger than 2*t*. There is a tradeoff between maximizing the fin surface area that experiences convective heat transfer and maximizing the *FF*. The minimum 2*t* is also governed by manufacturing constraints. Furthermore, the simplifying assumptions guarantee that the fin is sufficiently thin to ensure the Biot number is much less than unity. Therefore, 2*t* is maximized to the extent that the Biot number approaches 0.1, enabling the greatest A_c.

For the fluid flow velocity, a survey of commercially available electronics cooling fans provides an upstream air velocity (u_0) of 5.9 m/s. Applying conservation of mass to a control volume on the inlet of two TE fins spaced *s* apart yields an air velocity between the fins (u_f) of 13.6 m/s which corresponds to a Reynold's number (*Re*) of 1155. For flow between two parallel plates the laminar to turbulent transition occurs at *Re* = 2300[17].

Consequently, due to limitations of the upstream velocity, the flow between the blades for this analysis is considered to be laminar. An analytic model for forced convection of plate fin heat sinks[18] is therefore utilized to model the air flow of the F-TEC. For the plate fin heat sink model, the Reynolds number (Re_s) is defined as $Re_s = {u_f s \rho}/{\mu}$ where ρ is the density of air and μ is the viscosity of air. The fluid properties are determined utilizing the average film temperature of the optimized fin (~375 K) resulting in a Re_s of 577 which signifies developing flow. The Reynolds number is multiplied by the aspect ratio of the channel (s/W) to yield $Re^*_s = 44.44$. The Nusselt number (Nu_s) is then evaluated via:

$$Nu_s = \left[\left(\frac{Re_s^* Pr}{2} \right)^{-3} + \left(0.664 \sqrt{Re_s^*} Pr^{\frac{1}{3}} \sqrt{1 + \frac{3.65}{\sqrt{Re_s^*}}} \right)^{-3} \right]^{-\frac{1}{3}}, \text{ for } 0.26 \le Re_s^* \le 175$$

where Pr is the Prandtl number and Nu_s is determined to be 4.83. Finally, the average convective heat transfer coefficient for the blade used in this analysis is solved for via $h = {Nu_s k_{air}}/{s}$, yielding h = 154 W/m^{2}K.

2.6.2 Cold Side Heat Exchanger Thermal Resistance

The thermal insulance (I_T) of the CSHX is derived from the thermal resistance of the CSHX utilized by Pietrzyk[15] to model the performance of conventional flat-plate TECs. To compensate for differences in the *FF* between a F-TEC and a flat-plate TEC, the thermal resistance of Pietrzyk's CSHX is normalized to the A_{mod} of the flat-plate TEC times *FF* to derive the thermal insulance (I_T) in units of Km^2/W. **Table 1** contains the I_T utilized for the F-TEC CSHX. The R_{cs} utilized in this analysis is related to I_T by $R_{cs} = I_T / A_c$.

2.6.3 Key Model Parameters

Careful attention is paid to ensure that the material properties and operating conditions applied to the module represent available materials and achievable operating conditions, respectively. The thermal insulance of the CSHX is based upon fin performance characterized in literature.[19] The electrical interconnect resistance is considered negligible. The TE properties selected for this analysis are approximated from common bismuth telluride properties found in literature.[20, 21] The most relevant module parameters are presented in **Table 1**. The complete list of model parameters can be in found in Appendix A.2

Table 1 – Relevant model parameters

Parameter	Value
TE Electrical Conductivity, $\sigma\left[\frac{\mathrm{S}}{\mathrm{m}}\right]$	68200
TE Seebeck Coefficient, $S\left[\frac{\mu\mathrm{V}}{\mathrm{K}}\right]$	220
TE Thermal Conductivity, $k\left[\frac{\mathrm{W}}{\mathrm{mK}}\right]$	1.4
Material Figure-of-Merit, zT	0.7
Fin Thickness, $2t$ [mm]	1.3
CSHX Thermal Insulance, $I_T\left[\frac{\mathrm{Km}^2}{\mathrm{W}}\right]$	1.45E-4
Convective Heat Transfer Coefficient, $h\left[\frac{\mathrm{W}}{\mathrm{m}^2\mathrm{K}}\right]$	154
Biot Number, Bi_t	0.094
Ambient Temperature, $T_\infty\left[\mathrm{K}\right]$	298

CHAPTER 3. KEY FINDINGS

3.1 Fin Length and Insulation Length Optimization

The geometric optimization of F-TECs begins by investigating the impact on q_c'' of varying the insulation length at j = 0.91 A/mm^2 and L = 5 cm, over a range of thermal resistances (R) utilizing the 1D insulated derivation. The insulation length is a function of the cold side temperature which is dependent on R. **Figure 10 (a)** indicates that as a function of R, there exists an optimum fin insulation length ($L_{ins,opt}$) that maximizes q_c'' for a given power input. The black dashed lines in **Fig. 10(a)** and **(b)** represent the optimum insulation length as a function of R that maximizes q_c''. **Figure 10(b)** displays the insulation length temperature for a given insulation length and R. The optimum insulation length temperature is confirmed to always coincides with T_∞. As the thermal resistance increases, the optimum insulation length converges to a maximum value. **Figure 10(c)** depicts the temperature profile of the fins at the optimum insulation lengths (fins with insulation lengths corresponding to the black dashed lines) as a function of thermal resistance (R). Recalling that the cooler solution considers only a CSHX, R simplifies to R_{cs} at 8.6 K/W. The temperature profile as a function of fin position for the three R values (R_{cs}, R = 123 K/W, and R = 489 K/W) is depicted in **Fig. 10(d)**. As R approaches infinity, the cold side temperature converges to a minimum. As R decreases, as in the case of the cooler solution, L_{ins} also decreases. Values of L_{ins} for $R = R_{cs}$, through R = 489 K/W are determined numerically to be 0.18 mm, 1.03 mm, and 1.46 mm, respectively.

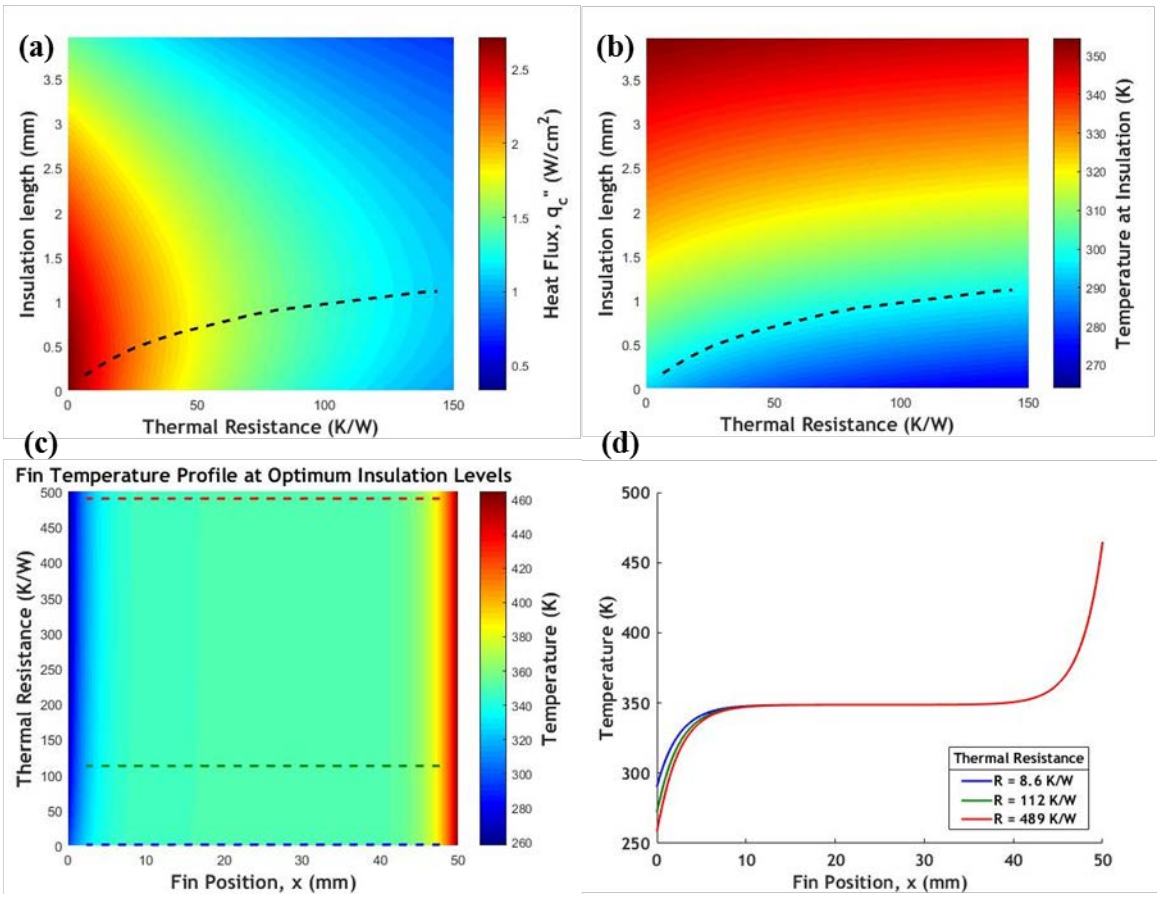

Figure 10 – (a) q_c'' and (b) temperature at insulation as a function of insulation length and R. The black dashed line represents the optimum insulation length that maximizes q_c'' for a given L. The optimum insulation length always occurs at T_∞. (c) The fin temperature profiles at the optimum insulation lengths. The fin temperature as a function of fin position for the blue (the case of $R = R_{cs}$), red, and green lines are plotted in (d). The green and red lines reveal the convergence of the T_c to a minimum as R increases.

Figure 11 depicts F-TEC performance as a function of L for both the 1D insulated and uninsulated derivations. As L increases, the q_c'' and L_{ins} of F-TECs converge to a maximum and T_c converges to a minimum. This behavior represents a significant deviation from conventional flat-plate TECs. Flat-plate TEC legs have an optimum leg height, increasing L beyond that optimum decreases q_c'' because the Joule heating term begins to dominate. However, for F-TECs at $L > L^*$, the additional fin length ($L - L^*$) is sufficient to reject the

additional Joule heating incurred by $L - L^*$ therefore $L > L^*$ does not decrease q_c'' or increase T_c. Comparing the simplified q_c'' F-TEC expression in **Eqn. 36** with that of the flat-plate, **Eqn. 1**, normalized to A_c, and substituting in $J = jA_c$ illustrates this point.

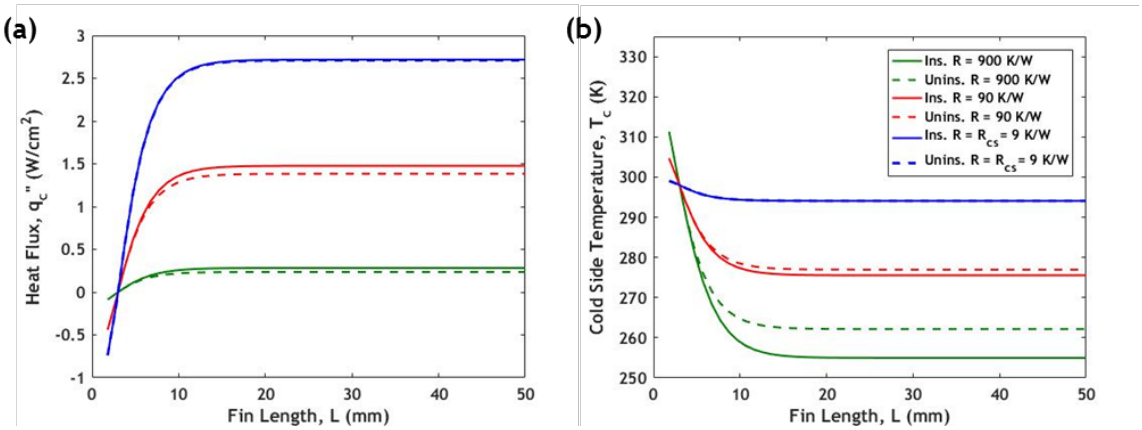

Figure 11 – As *L* increases (a) q_c'' converges to a maximum and (b) T_c converges to a minimum. In both (a) and (b), as *R* increases, differences between the performance of the insulated and uninsulated F-TECs are amplified. The magnitude of *R* must be considered when utilizing the optimum geometry approximations derived in section 2.5.3.

The simplicity of the uninsulated F-TEC analytical solution and the similitude of the performance to that of the insulated F-TEC makes the uninsulated model a useful tool to approximate critical device geometries. However, it is crucial to quantify when the approximations are valid. For every application of F-TECs, the cooled space will have some R_{ref} , and based on module design, a corresponding R_{ins}. As R_{ins} increases the q_c'' is limited causing the refrigerated space temperature and T_c to decrease. As T_c decreases, the optimum L_{ins} increases, and the impact of fin insulation on q_c'' is amplified, causing differences in the L that maximizes q_c'' between the models to increase. Therefore, the magnitude of R must be considered when applying the analytical simplifications derived in Section 2.5.3 to solve for the critical geometric dimensions of the insulated F-TEC.

Figure 12 quantifies the difference between utilizing the geometric design strategy for the critical dimensions (derived in Sections 2.4.3 and 2.5 and summarized in Appendix A.1) and utilizing **Eqn. 32** to solve for the insulated F-TEC $q''_{c,max}$ over a range of R.

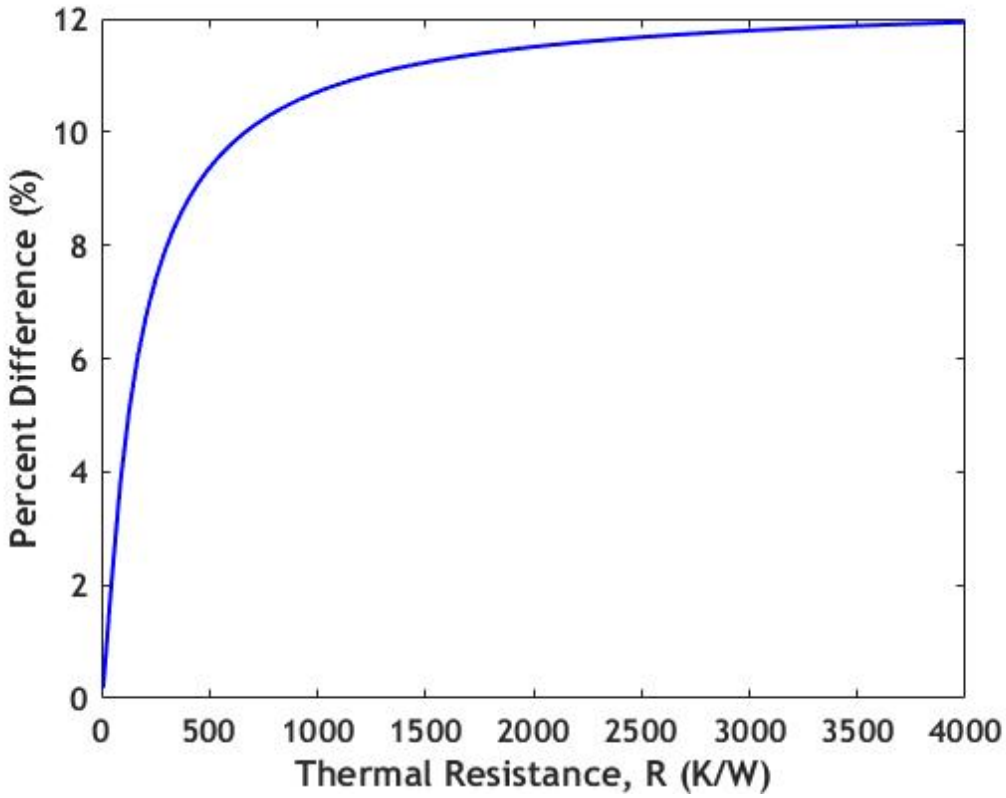

Figure 12 – Percent difference analysis of $q''_{c,max}$ calculated with the simplified analytical expressions for critical dimensions (Eqns. 53, 57, and 36) versus maximum q_c'' solved for with the insulated F-TEC solution (see Section 2.4.2) as a function of R.

Now that the impact of R on insulation length and device performance is demonstrated and the percent difference between the two approaches is demonstrated. All analysis is completed for the case of a TEC operating with only a CSHX attached, (*i.e.* $R_{ins} = 0$.) For the case of $R = R_{cs}$, the percent error of utilizing the approximations is 0.18%. **Figure 13** demonstrates q_c'' and COP as a function of L for a F-TEC with CSHX utilizing the full insulated and uninsulated derivations. Conversely to q_c'', there exists an optimum L that

maximizes *COP* for F-TECs, which is less than the *L* that maximizes q_c''. As *L* increases beyond the value that maximizes *COP*, the Joule heating begins to dominate and impair the *COP*. Additionally, at low *R*, the *COP* of the uninsulated and insulated F-TECs perform very similarly, indicating that the uninsulated model can determine the optimum *L* that maximizes *COP* for the insulated F-TEC. Finally, the leg height of flat-plate TECs is approximately 1 – 2 mm, **Fig. 13** demonstrates that at equivalent fin lengths, the q_c'' and *COP* are negative, indicating that convective heat transfer off the legs of flat-plate TECs is insufficient for adequate TEC device performance.

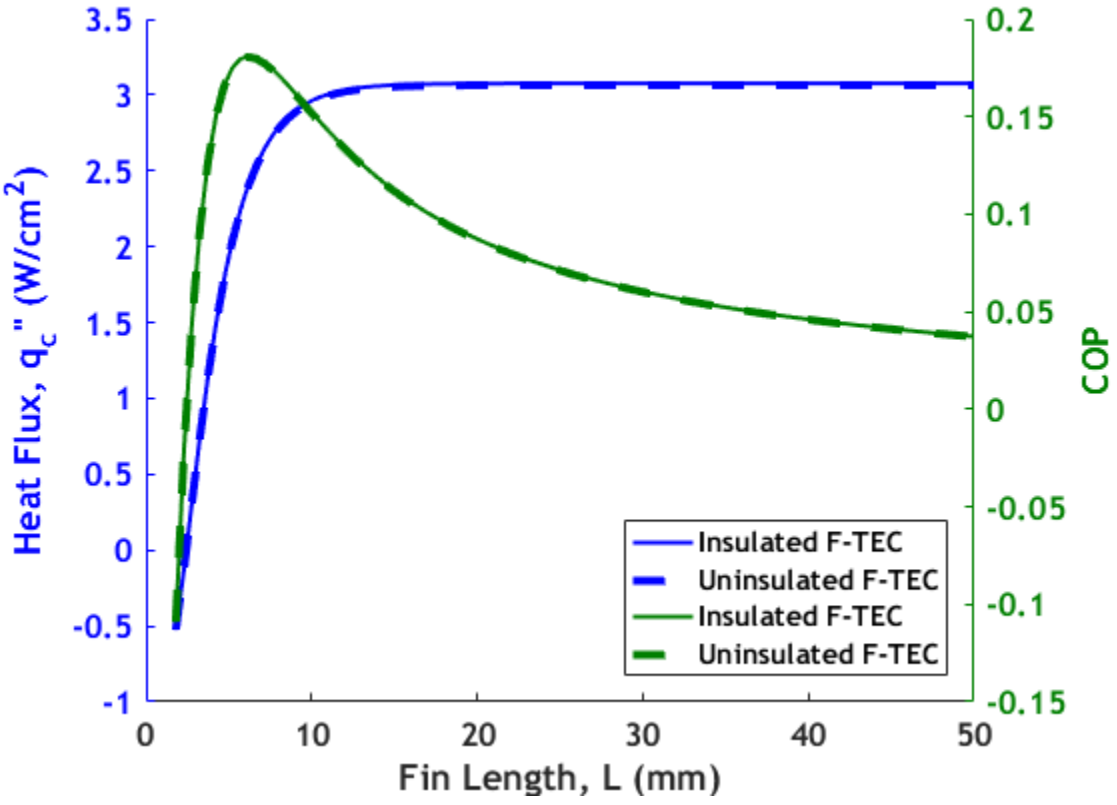

Figure 13 – q_c'' and *COP* as a function of *L* for the case of a F-TEC operating with only a CSHX attached (*R* = 8.6 K/W).

3.1.1 Optimized Geometric Dimensions

Now that the impact of L and L_{ins} on q_c'' is fully demonstrated, the optimum values are derived utilizing the simplified expressions of the geometric design strategy. In order to solve for the L^*, $q''_{c,U,max}$ must be found first. Utilizing **Eqn. 56**, $q''_{c,U,\max}$ is determined to be 2.710 W/cm^2. Utilizing **Eqn. 57**, L^* corresponding to 99.99% of $q''_{c,U,\max}$ is determined to be 2.60 cm. With L^* solved, **Eqn. 53** is finally utilized to determine $L_{ins,opt}$ to be 0.18 mm. Applying those dimensions to **Eqn. 37** yields the approximated q_c'' for the insulated F-TEC of 2.712 W/cm^2. Next, turning to the full evaluation of the insulated F-TEC model, **Eqn. 32** is utilized to solve for $q''_{c,max}$ = 2.717 W/cm^2. The L is selected that corresponds to 99.99% of $q''_{c,max}$ yielding, L = 2.60 cm, and the optimum L_{ins} is determined to be 0.18 mm. The percent difference between the insulated solution for $q''_{c,max}$ and the simplified expressions for the geometric dimensions for $q''_{c,max}$ is verified to be 0.18%

3.2 Impact of Fin Width on CS Heat Flux and COP

With L and L_{ins} now optimized, the impact of w on device performance is investigated. **Figure 14(a)** demonstrates the relationship between w and q_c'' utilizing the full 1D insulated F-TEC derivation. Holding j constant, for any given L, q_c'' is not dependent on w, as is demonstrated by **Eqn. 37** with $R = I_T A_c$. Additionally, **Fig. 15** demonstrates that COP is not a function of w. The width dimension is therefore free to be selected based upon the specific application constraints. For instance, w can be minimized if J must be limited; alternatively, w can be increased to increase Qc.

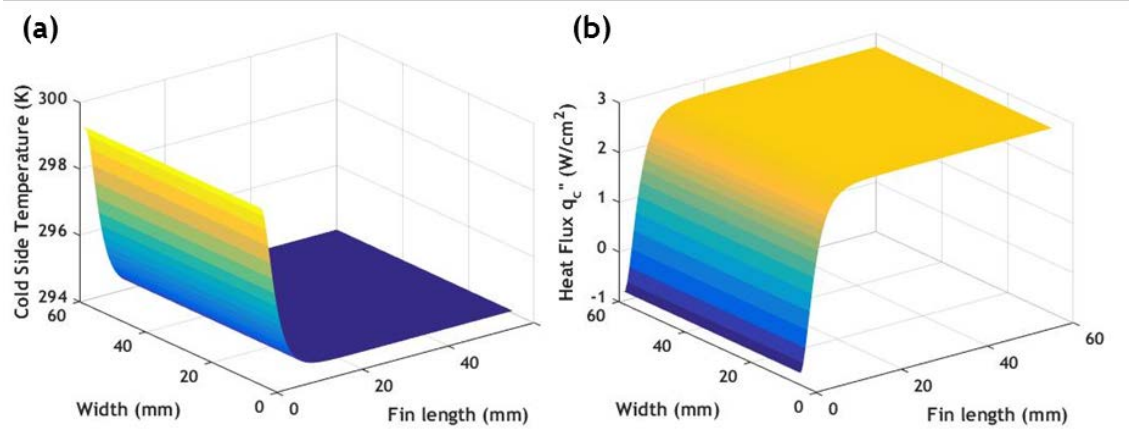

Figure 14 – At a fixed *j*, the F-TEC q_c'' and T_c are functions of *L* not *w*.

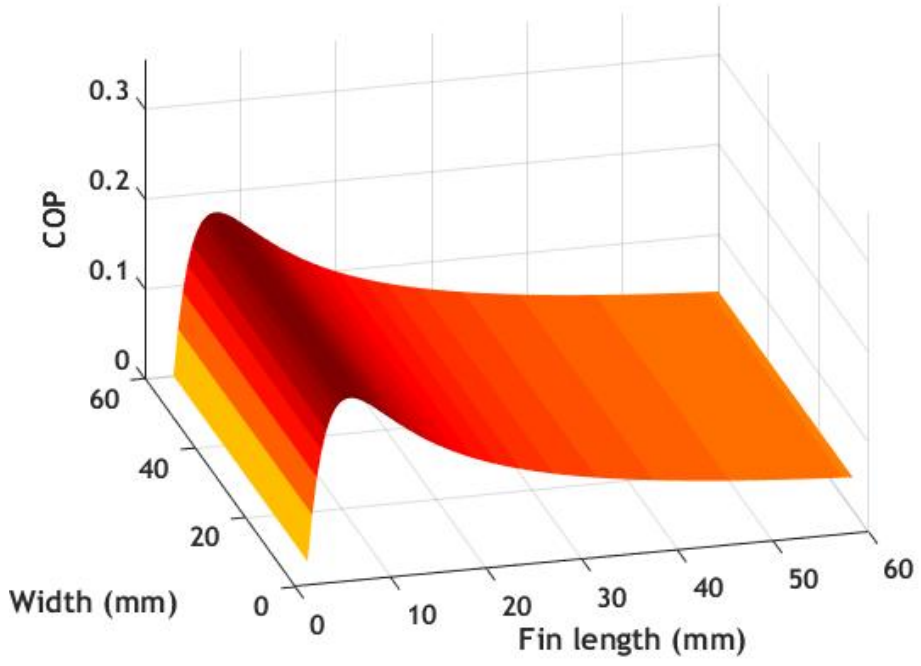

Figure 15 – COP as a function of fin *w* and *L*. Increasing *w* impacts Q_c and losses proportionally thereby leaving *COP* unaffected.

3.3 Impact of Current Density on CS Heat Flux and COP

Finally, the current density is optimized with w set to $10t$ in order to reduce the optimum current utilizing the 1D insulated F-TEC derivation. At L^*, the optimum current density that corresponds to $q''_{c,max}$ is identified to be 0.905 A/mm^2 (see **Fig. 16.**) The relationship between j and $q''_{c,max}$ for F-TECs is similar to conventional flat-plate TECs. As j increases beyond the optimum, Joule heating begins to dominate and inhibits q_c''. The COP as a function of current density is depicted below in **Fig. 16(b)**. As j increases, the corresponding L necessary to achieve the maximum COP also increases.

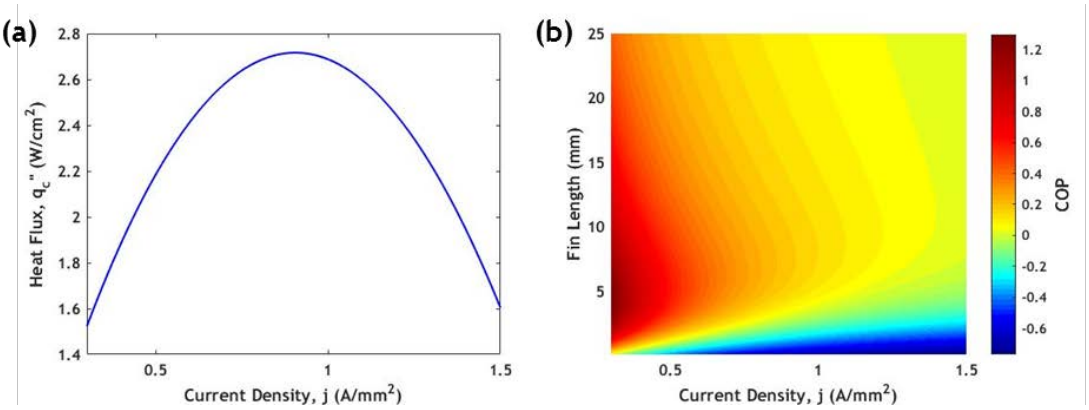

Figure 16 – (a) Heat flux as a function of current density at L^*, w, and $L_{ins,opt}$. (b) COP vs. j and L for F-TEC. As j increases, the L that maximizes COP also increases.

3.4 Impact of Convective Heat Transfer Coefficient on CS Heat Flux

With the optimum j and geometry determined, the impact of the convective heat transfer coefficient, h, on q_c'' is investigated next. Using the optimum geometry and j the impact of the convective heat transfer coefficient on q_c'' is demonstrated in **Fig. 17**. As h increases, convective heat transfer removes more of the Joule heating and the hot side Peltier heating, which reduces the amount of parasitic heat flowing to the cold side. The temperature

profiles of the fin subject to the three h values (**Fig. 17(b)**) confirms the removal of additional Joule heating in the body of the fin. At higher values of h, L^* decreases and COP is increased in two respects. First by increasing the q_c'' and second by the diminishing the P input.

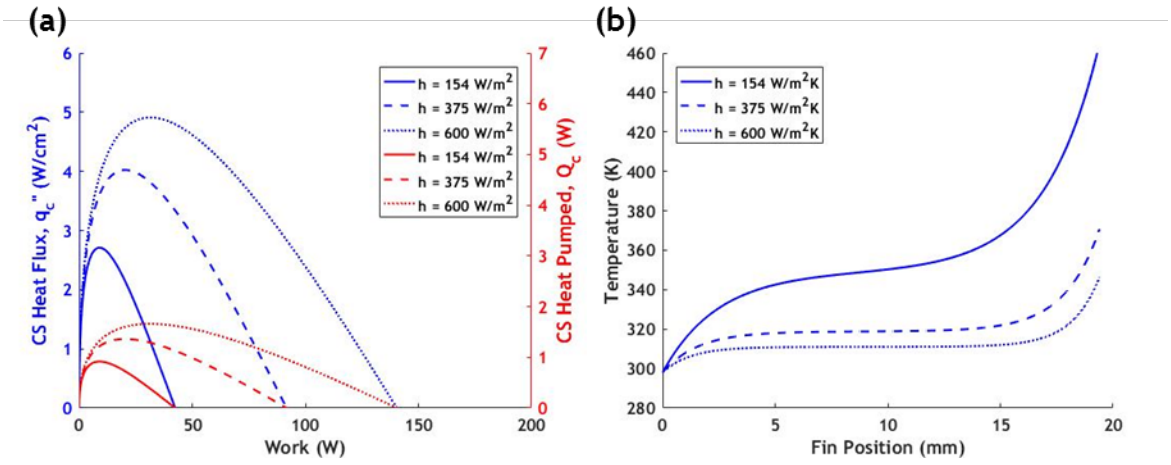

Figure 17 – (a) q_c'' and Q_c for a given power input at various h. (b) The impact of h on the temperature profile of the fin.

3.5 F-TEC / Conventional Flat Plate TEC Comparison

To conclude the analysis, the F-TEC is compared to a conventional flat-plate TEC that utilizes the same volume of TE material, to ensure the TE material cost is the same. For the F-TEC, as a result of q_c'' and COP being independent of w, and in order to minimize the required optimum current, $2w$ is set to 13 mm. A two-blade F-TEC module is considered with s set to 1 mm, 0.5 mm allotted on either end of the module, and the corresponding FF of 0.72. The optimum blade dimensions derived in Section 3.1.1 are utilized as well as the optimum j derived in Section 3.3. All other model parameters utilized are listed in **Table 1**. The 1D insulated F-TEC solution is utilized to quantify the F-TEC module performance. The conventional flat-plate TEC utilizes the same volume of

material as the F-TEC resulting in 47 legs. The leg width, thickness, and height are considered to be 2.2 mm x 2.2 mm x 1.5mm and the module has a commonly utilized *FF* of 0.33[15] which corresponds to common commercial TEC modules. The cold and hot side thermal insulances are considered to be 2.05×10^{-4} Km^2/W and 1.45×10^{-4} Km^2/W [15]. The TE properties and all other relevant parameters are identical to the F-TEC model. The module cold side heat flux ($q''_{c,mod}$) and heat pumped ($Q_{c,mod}$) by the F-TEC and conventional flat-plate TEC as a function of power input are depicted below in **Fig. 18.**

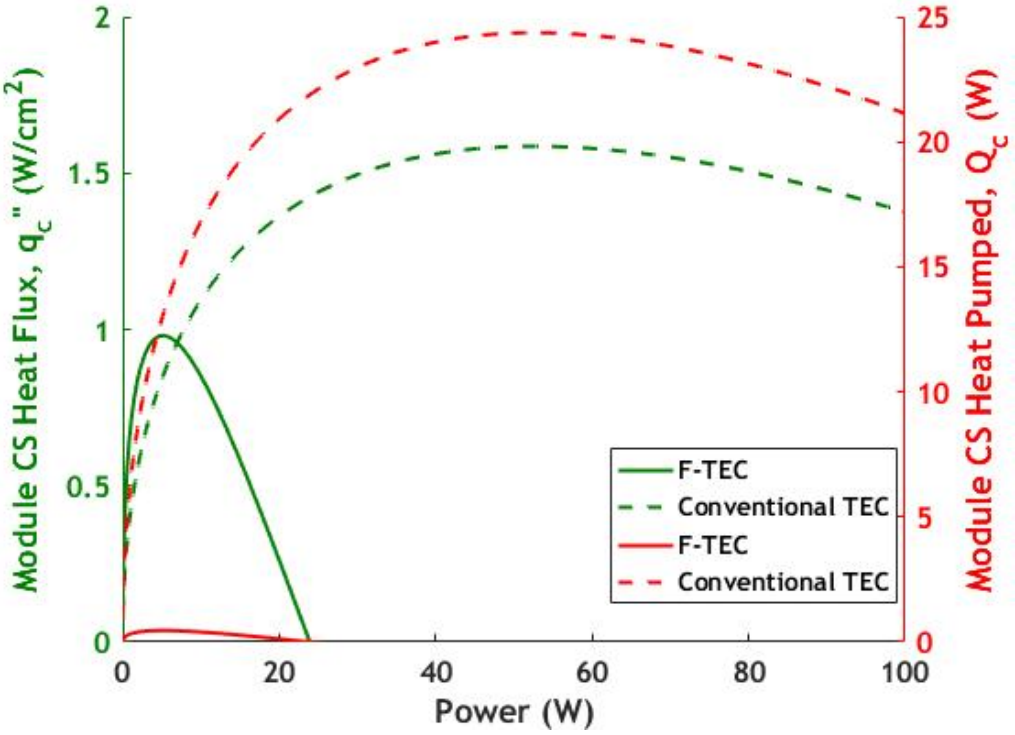

Figure 18 – Comparison of F-TEC and conventional flat-plate TEC $q''_{c,mod}$ and $Q_{c,mod}$ for a given power input (P). For 0 < P < ~ 7 W $q''_{c,mod}$ of the F-TEC is greater than the flat-plate TEC modeled.

For the constant TE material volume comparison of the F-TEC and flat-plate TEC the flat-plate TEC demonstrates higher overall $q''_{c,mod}$. However, over a low range of power input, the F-TEC $q''_{c,mod}$ is greater than that of the flat-plate TEC for a given power input.

However as the power input increases, the F-TEC is insufficient at rejecting the additional Joule heating and the hot side Peltier effect incurred thus $q''_{c,mod}$ begins to decrease, indicating that the hot side heat exchanger of the flat-plate TEC performs better than the F-TEC. While the $q''_{c,mod}$ is comparable between the F-TEC and flat-plate TEC, the F-TEC utilizes most of the TE material to increase the blade length to reject heat, while the flat-plate TEC utilizes most of the material to increase the cross-sectional area of the TE material in the module. Consequently, for a constant volume comparison of flat-plate TEC and F-TEC coolers, the flat-plate TEC pumps significantly more heat (Q_c) for a given work input.

Lastly, **Fig. 18** can be utilized to validate the assumption that the fan power requirements have negligible impact on the *COP*. The electronic cooling fan power requirements (experimentally approximated to be 3 W) normalized to the area of the fan (64 cm) can be utilized to estimate the fan power consumption per F-TEC couple. Consequently, the F-TEC module utilized in the flat-plate comparison requires 0.022 W of auxiliary power for the cooling fan, which represents less than 5% of the total heat pumped and 0.4% of the F-TEC power input. However, the impact of the pressure drop across the blades on the cooling fan power requirements and the fan velocity should be considered in future work.

CHAPTER 4. MODEL VALIDATION

4.1 Constant Convective Heat Transfer Coefficient COMSOL Model

The 1D F-TEC analytical model is validated against a COMSOL model of the F-TEC operating under two different convective heat transfer coefficient (h) conditions. The first COMSOL model maintains that h is spatially constant across the entire surface of the fin and is set to 154 W/m^{2}K in this case. The second COMSOL model enables forced airflow across the blades to assess the efficacy of the constant h assumption. For the first case, the 1D analytical model and the COMSOL model are compared over a range of w and L. With constant h, the temperature profile of the optimized geometry F-TEC is depicted below in **Fig. 19**.

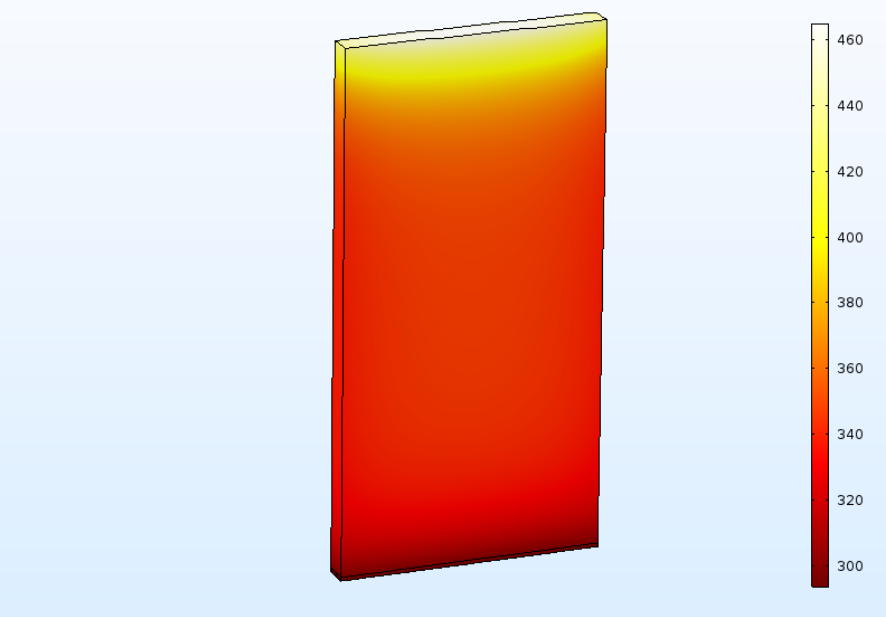

Figure 19 – Temperature Profile of the F-TEC at the optimized geometry and current density (j) with h = 154 W/m^{2}K.

For the optimized fin geometry, the 1D analytical model over predicts T_c and T_h compared to the surface average temperatures determined by COMSOL by 0.03% and 1.6%, respectively, and under predicts q_c'' by 2.16%. Indicating that the 1D model is a slightly conservative estimate of the F-TEC q_c''. The impact of varying w on q_c'' is depicted in **Fig. 20** below.

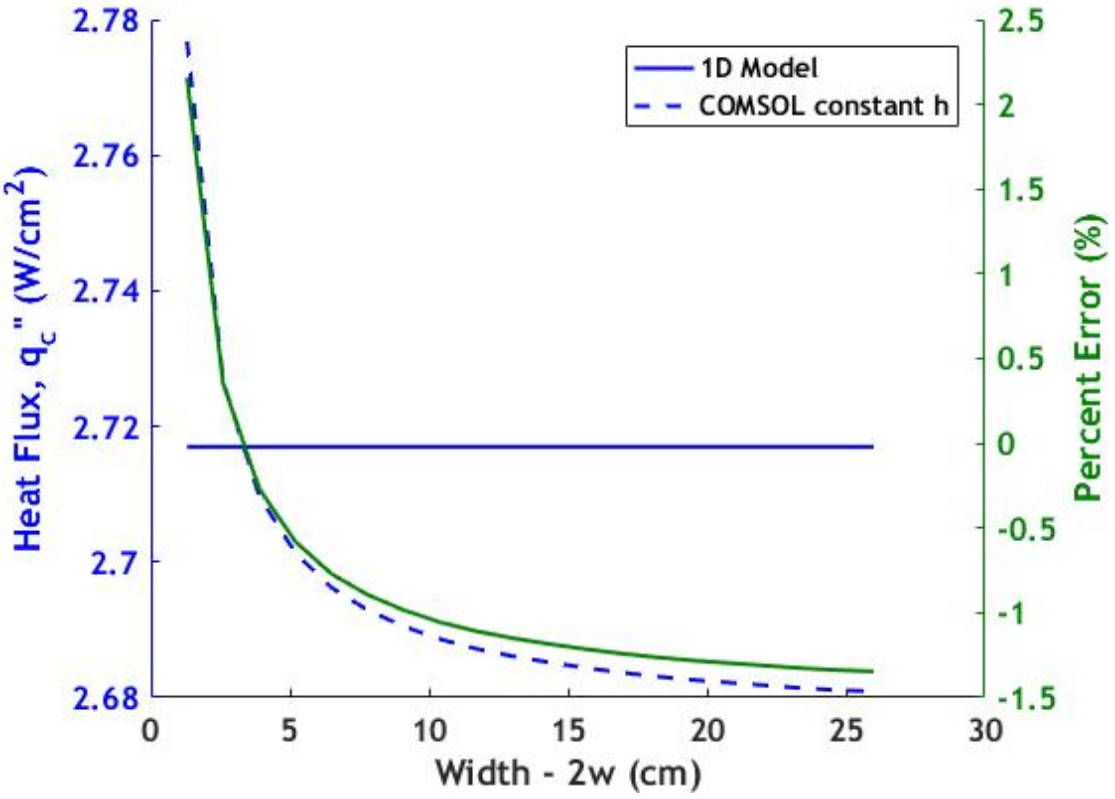

Figure 20 – q_c'' and percent difference for the 1D analytical and the COMSOL model as a function of 2*w*.

The q_c'' of COMSOL model converges as w increases, differing from the 1D analytical model, which is constant as the width changes. The models converging as w increases indicates that the difference is likely due to the simplifying assumption that the perimeter could be reduced from $4w + 4t$ to $4w$. However, the percent error between the two models

is at most 2.25% rendering the difference relatively negligible. Finally, q_c'' of the COMSOL and 1D analytical models are compared as L varies in **Fig. 21**.

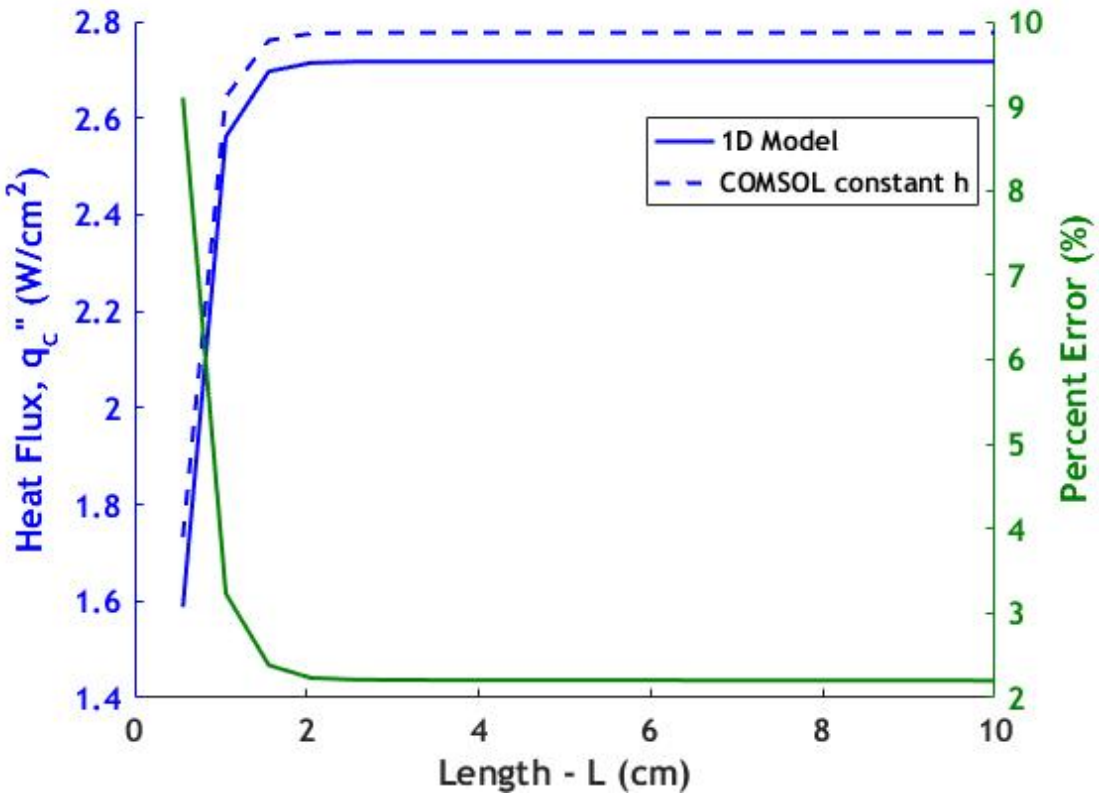

Figure 21 – q_c'' and percent difference for the 1D analytical and the COMSOL model as a function of L.

Both models confirm that as L increases, q_c'' converges to a maximum. There is greater difference between the models when L is not sufficiently long, but assuming the q_c'' is maximized for a given power input, the percent error between the models converges to 2.16%. The minimal difference in the q_c'' between the models verifies that there is minimal temperature variation in the y-direction and that the quasi-1D heat transfer assumption is a valid simplification.

4.2 Validity of Constant Convective Heat Transfer Coefficient Assumption

The second COMSOL model considers performance when *h* is not spatially constant or temperature independent. To model flow over the F-TEC, two blades are located in air flow with an inlet velocity of 5.9 m/s and are spaced 1 mm apart. Symmetry is applied to both the fin and the air flow. The upper flow boundary is set to 1 mm above the hot side of the fin, to ensure similar convective heat transfer off that region as the body of the fin, and to prevent air flow from decreasing between the fins. This boundary is accomplished in practice by surrounding the fins with an aluminum shield that forces flow between the blades. Temperature and flow velocity profiles for the optimized geometry fin are depicted below in **Fig. 22** and **Fig. 23**.

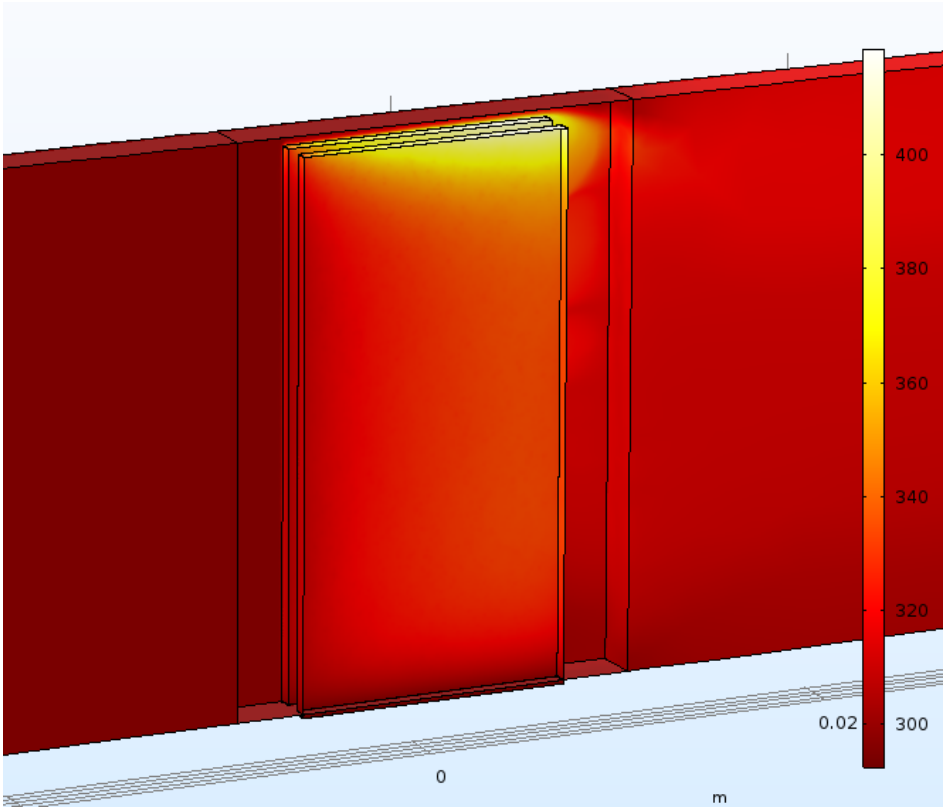

Figure 22 – Temperature profile of optimum geometry F-TEC in the forced air flow COMSOL model.

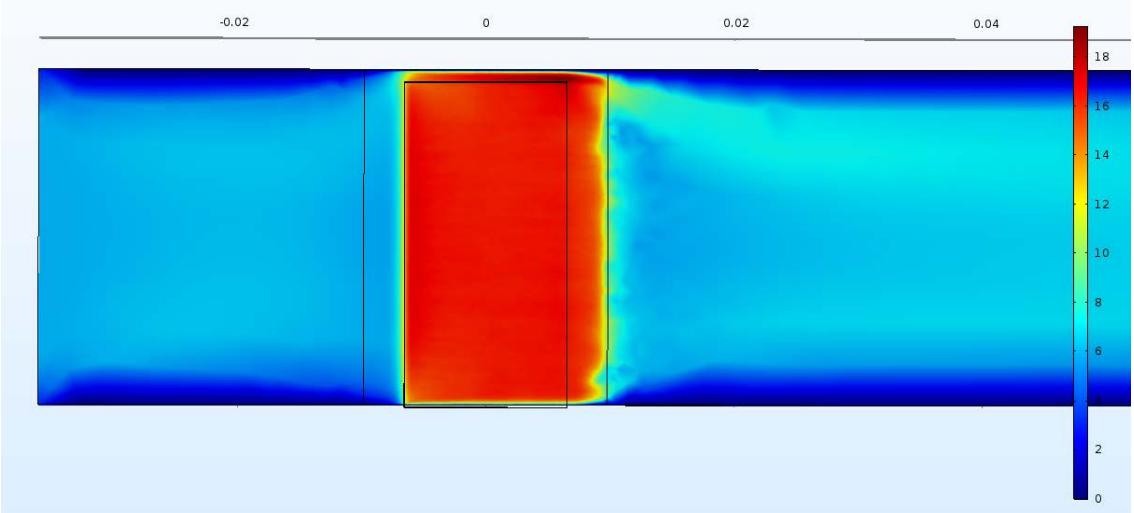

Figure 23 – Velocity profile of air flow over the optimum geometry F-TEC.

As the mesh becomes finer the fluid flow convective heat transfer model begins to converge to the 1D model. **Figure 23** confirms the fin air velocity (u_f) selected for this analysis and that the flow tunnel surrounding the blades is sufficiently larger than the blades to ensure that the inlet and outlet boundary conditions do not alter the velocity profile. Three flow regions are generated to enable a finer mesh surrounding the blades. When the maximum element size in the blade section reaches 185 μm, the 1D model under predicts the surface average T_h by 18.2%, and surface average T_c by 0.3%, and over predicts q_c'' by 16.7%. Computational limitations inhibited further reductions of the mesh size. Based on the fluid flow COMSOL model, the convective heat transfer coefficient simplifications utilized in the 1D model are a valid representation of heat transfer in a F-TEC at the optimum length scale. Further study is necessary to validate how efficacious the convective heat transfer simplifications are as the width increases.

Despite the similitude between the average hot side temperatures in the 1D and COMSOL models, the temperature profile of the blade hot side in COMSOL is skewed to the trailing edge of the blade as depicted in **Fig. 24**.

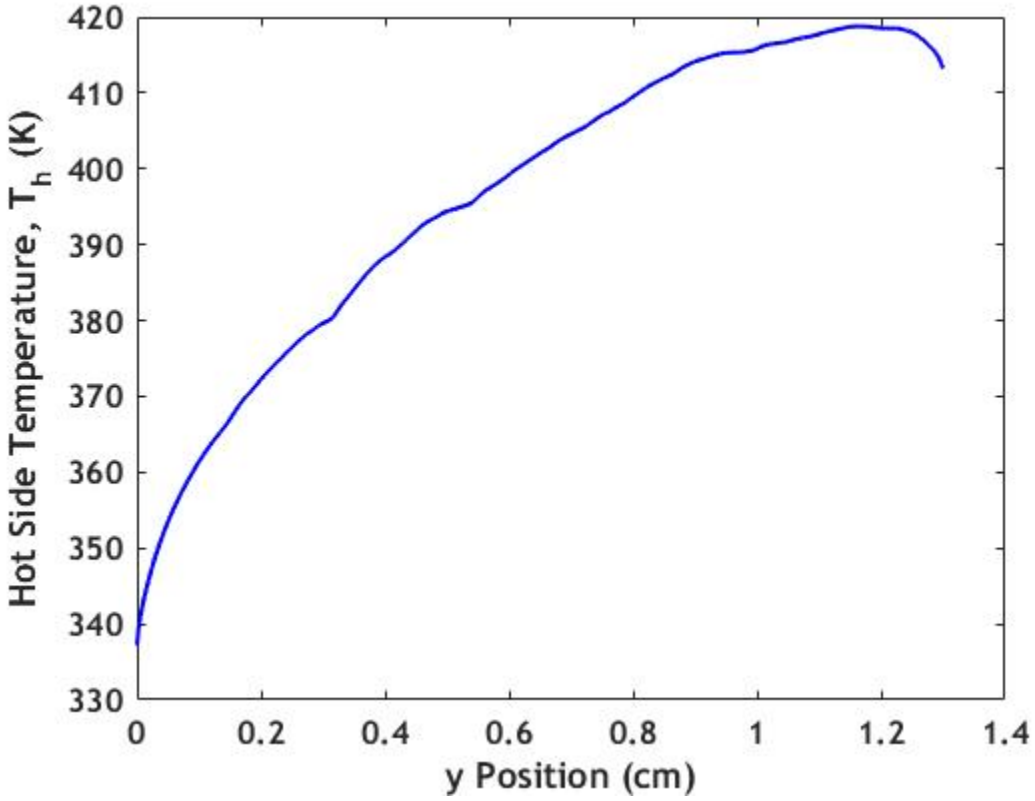

Figure 24 – Hot side temperature profile of optimum geometry blade.

Variation in the hot side temperature profile is likely the result of three causes. First, the flow is not fully-developed in the initial region resulting in an amplified local convective heat transfer coefficient in this region. Second, the ambient temperature surrounding the blade towards which heat is convecting increases as the flow progresses through the blades, resulting in less heat being transferred. Lastly, the properties of the air are temperature dependent, causing further variation as the flow progresses. The same variation is not seen

in the cold side temperature profile as can be inferred from the small percent difference between models.

CHAPTER 5. CONCLUSION

Thermoelectric cooling enables the direct conversion of electricity to cooling. There are many applications for TECs ranging from traditional refrigeration to electric vehicles and electronics. Developing TECs that operate more efficiently, at higher q_c'', and inexpensively is necessary to make TECs viable on a large scale for these applications. Device architecture and system design play a significant role in device performance [11, 13], further, conventional flat-plate TEC system design is dominated by the cost of the heat exchangers.[14] F-TECs address the later problem by eliminating the need of the hot side heat exchanger. The aim of this thesis was to model F-TEC device performance (*i.e.*, q_c'' and *COP*) as it relates to the device geometry and power input. Significant contributions of this work include developing the heat transfer models for insulated and uninsulated F-TECs, deriving closed-form analytical expressions for optimum device geometry, and finally optimizing F-TEC *COP* and q_c''.

F-TECs perform differently than conventional flat-plate TECs. First, there is not an optimum L that maximizes the q_c'' of F-TECs. Rather q_c'' asymptotically approaches a maximum as L increases. Additionally, by increasing the convective heat transfer coefficient (h), F-TECs can potentially generate larger heat fluxes than their flat-plate TEC counterparts with a similar h because there is less volumetric Joule heating, and conduction from the hot to cold side, which inhibits q_c''. The most significant contribution of F-TECs is the elimination of the hot side heat exchanger. While Q_c and *COP* are lower for the F-TEC when compared to a flat-plate TEC for an equivalent volume of TE material, the F-TEC has the distinctive advantage as a system because it requires one less heat exchanger.

Therefore, future work could include completing a F-TEC system cost analysis to determine what cost-performance tradeoffs may exist.

Additionally, the performance of a F-TEC should be analyzed experimentally. A F-TEC module can be manufactured by slicing bismuth telluride TE material into blades with a wire EDM. The hot and cold side surfaces can be prepared for solder by electroplating silver and nickel on both surfaces. A plastic mold can then be utilized to hold the blades in place while assembling and soldering the cold side of the module. A preform can be utilized to slice slots for the blades into the thermal insulation, which can then slide over the blades after the cold side is soldered. Finally, electrical interconnects can be soldered onto the fin hot side. A shroud oriented in the direction of the air flow should encapsulate the F-TEC blades to ensure the maximum flow between the blades.

APPENDIX A.

A.1 F-TEC Geometric Design Strategy to Maximize CS Heat Flux Utilizing Closed-form Expressions for Critical Dimensions

Optimization of F-TECs is always application dependent. Design targets for *COP* and q_c must be considered, both of which are dependent on the area available for TE modules to cover as well as the thermal resistance of the refrigerated space insulation (R_{ins}). Additionally, capabilities of the power supply must be taken into account. A heat exchanger for the cold side must be selected, and a method of forcing convection on blades must be determined, as well as the corresponding convective heat transfer coefficient (h) for the fin hot side. For a given j, A_c, and s the necessary equations that optimize device geometry to maximize q_c'' from Sections 2.4 and 2.5 are summarized in Table 2 with R substituted in for R_{cs}. The procedure is detailed below:

1. Solve **Eqn. 56** for the uninsulated F-TEC maximum CS heat flux ($q''_{c,U,max}$).
2. Select χ (such that $0 < \chi < 1$) to solve for L^* that corresponds to $\chi \cdot q''_{c,U,max}$ utilizing **Eqns. 57** through **59** and the necessary supplemental equations found in Section 2.5.2.
3. Solve **Eqn. 53** for the optimum insulation length ($L_{ins,opt}$.)
4. Lastly, **Eqn. 37** is utilized to solve for the $q''_{c,max}$ of the insulated F-TEC.

Table 2 – Equations to optimize device geometry to maximize q_c''

Equation	Equation Number
$$q''_{c,U,max} = \frac{B/A - m}{A_c R}$$	**Eqn. 56**
$$L^* = \sqrt{\frac{kt}{h}} \ln\left(\frac{-\tau_2 \pm \sqrt{\tau_2^{\,2} - 4\left(BG + AG\tau_1\right)\left(-DF\tau_1 - BF\right)}}{2\left(BG + AG\tau_1\right)} \right)$$	**Eqn. 57**
$$\tau_1 = -\chi A_c R q''_{c,U,\max} - j^2 \rho t / h$$	**Eqn. 58**
$$\tau_2 = AE - DE$$	**Eqn. 59**
$$L_{ins,opt} = -\sqrt{\frac{kt}{h}} \ln\left(\frac{A}{B} \frac{j^2 \rho t}{h} \right)$$	**Eqn. 53**
$$q_c'' = \frac{jST_\infty - \frac{1}{2} j^2 L_{ins} \rho}{1 + jA_c SR + kA_c R / L_{ins}}$$	**Eqn. 37**

A.2 Additional Model Parameters

Properties necessary for the analysis of the convective heat transfer coefficient for flow between two flat parallel plates are in **Table 3**.

Table 3 – Additional model parameters

Parameter	Value
Density of Air, $\rho_{air}\left[\frac{kg}{m^3}\right]$	0.993
Viscosity of Air, $\mu\left[\frac{Ns}{m^2}\right]$	21.915×10^{-6}
Prandtl Number, Pr	0.695
Thermal Conductivity of Air, $k_{air}\left[\frac{W}{\mathrm{mK}}\right]$	0.0319

REFERENCES

1. Snyder, G.J. and E.S. Toberer, *Complex thermoelectric materials.* Nature Materials, 2008. **7**: p. 105.

2. Angrist, S.W., *Direct energy conversion*. 2d ed.. ed. 1971, Boston: Boston, Allyn and Bacon.

3. Menon, A.K. and S.K. Yee, *Design of a polymer thermoelectric generator using radial architecture.* Journal of Applied Physics, 2016. **119**(5): p. 055501.

4. Zhang, X. and L.-D. Zhao, *Thermoelectric materials: Energy conversion between heat and electricity.* Journal of Materiomics, 2015. **1**(2): p. 92-105.

5. Chen, Z.-G., et al., *Nanostructured thermoelectric materials: Current research and future challenge.* Progress in Natural Science: Materials International, 2012. **22**(6): p. 535-549.

6. Alam, H. and S. Ramakrishna, *A review on the enhancement of figure of merit from bulk to nano-thermoelectric materials.* Nano Energy, 2013. **2**(2): p. 190-212.

7. Snyder, G.J., et al., *Disordered zinc in Zn4Sb3 with phonon-glass and electron-crystal thermoelectric properties.* Nature Materials, 2004. **3**: p. 458.

8. Venkatasubramanian, R., et al., *Thin-film thermoelectric devices with high room-temperature figures of merit.* Nature, 2001. **413**: p. 597.

9. Heremans, J.P., et al., *Enhancement of Thermoelectric Efficiency in PbTe by Distortion of the Electronic Density of States.* Science, 2008. **321**(5888): p. 554-557.

10. Zhao, L.-D., et al., *Ultralow thermal conductivity and high thermoelectric figure of merit in SnSe crystals.* Nature, 2014. **508**: p. 373.

11. Fabián-Mijangos, A., G. Min, and J. Alvarez-Quintana, *Enhanced performance thermoelectric module having asymmetrical legs.* Energy Conversion and Management, 2017. **148**: p. 1372-1381.

12. Koichi, I., et al., *Fabrication of flexible thermopile generator*. Journal of Micromechanics and Microengineering, 2005. **15**(9): p. S233.

13. Owoyele, O., S. Ferguson, and B.T. O'Connor, *Performance analysis of a thermoelectric cooler with a corrugated architecture.* Applied Energy, 2015. **147**: p. 184-191.

14. Yee, S.K., et al., *$ per W metrics for thermoelectric power generation: beyond ZT*. Energy & Environmental Science, 2013. **6**(9): p. 2561-2571.

15. Pietrzyk, K., et al., *Thermoelectric module design strategy for solid-state refrigeration.* Energy, 2016. **114**: p. 823-832.

16. Incropera, F.P., *Fundamentals of heat and mass transfer*. 7th ed. 2011, Hoboken, NJ: John Wiley. xxiii, 1048 p.

17. Ghiaasiaan, S.M., *Convective heat and mass transfer*. 2011, Cambridge University Press,: Cambridge ; New York. p. xxiv, 524 p.

18. Teertstra, P., et al. *Analytical forced convection modeling of plate fin heat sinks*. in *Fifteenth Annual IEEE Semiconductor Thermal Measurement and Management Symposium (Cat. No.99CH36306)*. 1999.

19. Astrain, D., et al., *A comparative study of different heat exchange systems in a thermoelectric refrigerator and their influence on the efficiency*. Vol. 103. 2016.

20. Lowhorn, N.D., et al., *Development of a Seebeck coefficient Standard Reference Material™*. Journal of Materials Research, 2011. **26**(15): p. 1983-1992.

21. Parker, W.J. and R.J. Jenkins, *Thermal conductivity measurements on bismuth telluride in the presence of a 2 MeV electron beam.* Advanced Energy Conversion, 1962. **2**: p. 87-103.